Diverse Characteristics of Extreme Orographic Snowfall Events in Little Cottonwood Canyon, Utah

MICHAEL L. WASSERSTEIN[a] AND W. JAMES STEENBURGH[a]

[a] *Department of Atmospheric Sciences, University of Utah, Salt Lake City, Utah*

(Manuscript received 12 September 2023, in final form 28 January 2024, accepted 1 February 2024)

ABSTRACT: Heavy orographic snowfall can disrupt transportation and threaten lives and property in mountainous regions but benefits water resources, winter sports, and tourism. Little Cottonwood Canyon (LCC) in northern Utah's Wasatch Range is one of the snowiest locations in the interior western United States and frequently observes orographic snowfall extremes with threats to transportation, structures, and public safety due to storm-related avalanche hazards. Using manual new-snow and liquid precipitation equivalent (LPE) observations, ERA5 reanalyses, and operational radar data, this paper examines the characteristics of cool-season (October–April) 12-h snowfall extremes in upper LCC. The 12-h extremes, defined based on either 95th percentile new snow or LPE, occur for a wide range of crest-level flow directions. The distribution of LPE extremes is bimodal with maxima for south-southwest or north-northwest flow, whereas new-snow extremes occur most frequently during west-northwest flow, which features colder storms with higher snow-to-liquid ratios. Both snowfall and LPE extremes are produced by diverse synoptic patterns, including inland-penetrating or decaying atmospheric rivers from the south through northwest that avoid the southern high Sierra Nevada, frontal systems, post-cold-frontal northwesterly flow, south-southwesterly cold-core flow, and closed low pressure systems. Although often associated with heavy precipitation in other mountainous regions, the linkages between local integrated water vapor transport (IVT) and orographic precipitation extremes in LCC are relatively weak, and during post-cold-frontal northwesterly flow, highly localized and intense snowfall can occur despite low IVT. These results illustrate the remarkable diversity of storm characteristics producing orographic snowfall extremes at this interior continental mountain location.

SIGNIFICANCE STATEMENT: Little Cottonwood Canyon in northern Utah's central Wasatch Range frequently experiences extreme snowfall events that pose threats to lives and property. In this study, we illustrate the large diversity of storm characteristics that produce this extreme snowfall. Meteorologists commonly use the amount of water vapor transport in the atmosphere to predict heavy mountain precipitation, but that metric has limited utility in Little Cottonwood Canyon where heavy snowfall can occur with lower values of such transport. Our results can aid weather forecasting in the central Wasatch Range and have implications for understanding precipitation processes in mountain ranges throughout the world.

KEYWORDS: Atmosphere; Complex terrain; North America; Extreme events; Precipitation; Snow

1. Introduction

Orographic precipitation extremes in the form of heavy rainfall, snowfall, or other forms of precipitation can produce wide-ranging geophysical hazards and societal impacts including flooding (Maddox et al. 1978; Ralph et al. 2006; Neiman et al. 2011; Froidevaux and Martius 2016), avalanches (Schweizer et al. 2003, 2009; Farestveit and Skutlaberg 2009; Conlan and Jamieson 2016a,b), landslides (Johnston et al. 2021), structural collapses (Hilker et al. 2009), power outages (Roebber and Gyakum 2003), and immobilized transportation (Nöthiger and Elsasser 2004). Such extremes occur frequently during moist flow over hills and mountains with orographic lift enhancing precipitation rates through processes that include seeder–feeder and potential instability release (Roe 2005; Houze 2012; Colle et al. 2013; Stoelinga et al. 2013). Orographic precipitation extremes have been linked to atmospheric rivers (Neiman et al. 2011; Lavers and Villarini 2013; Froidevaux and Martius 2016; Lorente-Plazas et al. 2018), convective storms (Caracena et al. 1979; Wulfmeyer et al. 2011; Casaretto et al. 2022), lake- and sea-effect precipitation (Manabe 1957; Campbell et al. 2018; Veals et al. 2020; Steenburgh and Nakai 2020), extratropical cyclones (Lackmann and Gyakum 1999; Pandey et al. 1999; Viale and Nuñez 2011), and tropical cyclones (Smith et al. 2009; DeHart and Houze 2017), including those undergoing extratropical transition (Sinclair 1993; Sturdevant-Rees et al. 2001; Stohl et al. 2008; Liu and Smith 2016; Lentink et al. 2018). Often, the intensity and spatial distribution of orographic precipitation is closely related to the wind (or vapor transport) direction, with precipitation heaviest along or upstream of ridgelines that are aligned orthogonal to the flow (Houze et al. 2001; James and Houze 2005; Yuter et al. 2011; Foresti et al. 2018). For many regions—such as North America's Cascade Range, Olympic Mountains, and Sierra Nevada, or the European Alps—distinct synoptic patterns directly influence the location of extreme orographic precipitation (e.g., Pandey et al. 1999;

Supplemental information related to this paper is available at the Journals Online website: https://doi.org/10.1175/MWR-D-23-0206.s1.

Corresponding author: Michael L. Wasserstein, michael.wasserstein@utah.edu

DOI: 10.1175/MWR-D-23-0206.1

Minder et al. 2008; Yuter et al. 2011; Froidevaux and Martius 2016); in contrast, *several* different synoptic types can produce orographic precipitation extremes in some regions like Italy's Apennine Range (e.g., Capozzi et al. 2022).

Cool-season orographic snowfall extremes occur frequently in the Wasatch Range of northern Utah, a narrow, quasi-meridionally oriented mountain range at the eastern periphery of the Great Basin in the interior western United States (Figs. 1a,b). The Wasatch Range broadens east of the Salt Lake Valley where a series of zonally oriented ridges (Alpine, Cottonwood, and Wildcat) and canyons [Little Cottonwood Canyon (LCC), Big Cottonwood Canyon (BCC), and Mill Creek Canyon (MCC)] compose a significant portion of what is known locally as the central Wasatch Range (hereinafter central Wasatch; Fig. 1c). Little Cottonwood Canyon splits the Alpine and Cottonwood ridges, which rise to ~3300 m MSL, more than 2000 m above the Salt Lake Valley and Great Salt Lake (GSL). Mean cool-season (October–April) snowfall and liquid precipitation equivalent (LPE) [both based on daily NWS Cooperative Observer Program (COOP) station reports] increase from 207 cm and 432 mm at Cottonwood Weir (CW; see Fig. 1c; 1520 m MSL) at the western base of the central Wasatch to 1106 cm and 902 mm at Alta (2655 m MSL) in upper LCC (NCEI 2021). The snowfall and LPE increase with elevation reflect orographic enhancement, with the snowfall increase also affected by a greater fraction of precipitation falling as snow at upper elevations, which is near 100% at and above 2600 m MSL (Steenburgh 2023).

Within LCC, a two-lane highway, State Route 210 (SR-210), is the only transportation link to Alta. The road climbs 1000 m in 13 km, crossing 50 avalanche paths that leave it vulnerable to avalanches during frequent cool-season storms (Steenburgh 2023). Due to heavy traffic volumes, a lack of avalanche defense structures, and the large concentration of avalanche paths, SR-210 has the highest uncontrolled avalanche hazard index of any major road in the world (Schaerer 1989; Nalli and Mckee 2018). During and after periods of heavy snowfall, which is the strongest forecasting parameter for large new-snow avalanches (e.g., Foehn et al. 2002; Schweizer et al. 2003), dangerous avalanche conditions can force the closure of SR-210, threaten lives and property in the town of Alta and nearby village of Snowbird, and induce travel restrictions known as interlodge during which residents and visitors are legally mandated to remain indoors (Steenburgh 2023); during a particularly intense storm in February 2020, interlodge lasted for 52 consecutive hours. During the 2022/23 cool season, extreme snowfall and avalanches forced frequent multiday closures of SR-210, stranding residents and visitors and leading to food shortages (Jag 2023). The estimated revenue loss for ski areas and other businesses in upper LCC during the closure of SR-210 was \$1.4 million day^{-1} in the 1991/92 season (Blattenberger and Fowles 1995), or about \$3 million day^{-1} in 2023 dollars.

Snowfall in the central Wasatch can be produced by 1) unstable, post-cold-frontal northwesterly flow, 2) cold-frontal passages, 3) decaying or inland-penetrating atmospheric rivers, 4) localized lake-effect convection, and 5) closed upper-level low pressure systems (Dunn 1983; Carpenter 1993; Horel and Gibson 1994; Steenburgh 2003; Rutz and Steenburgh 2012; Alcott et al. 2012;

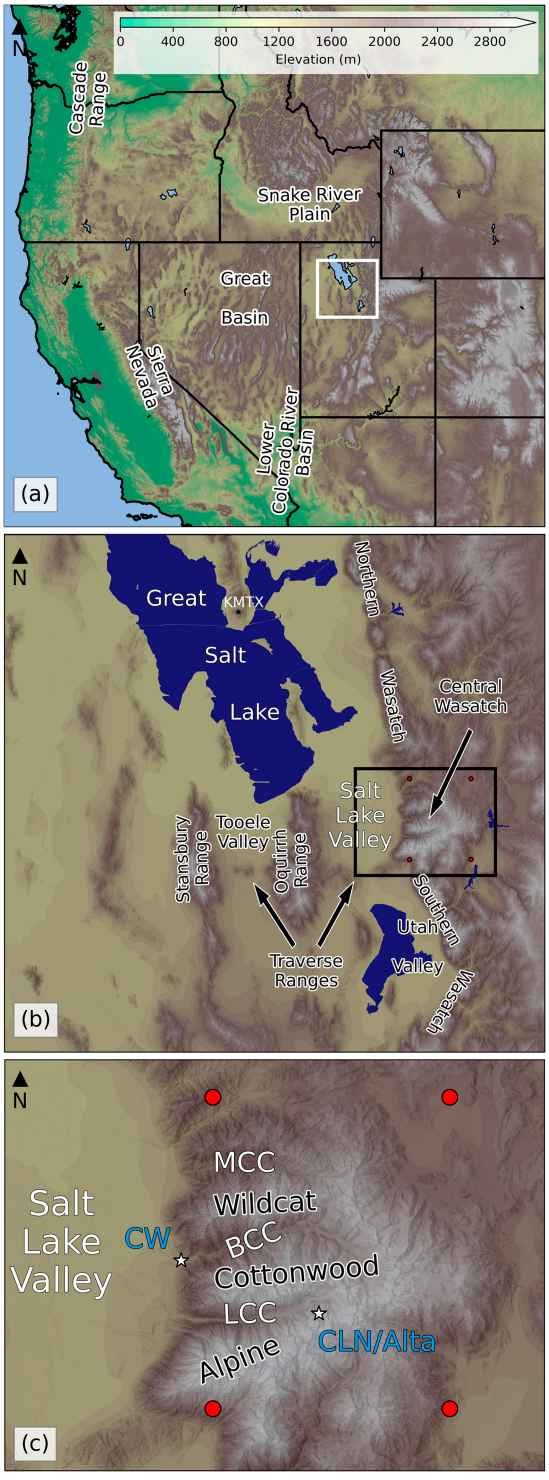

FIG. 1. Topography of (a) the western United States (scale at top), (b) the central Wasatch and surrounding region [identified by the white box in (a)], and (c) the central Wasatch [identified by the black box in (b)] with key geographic features annotated and four ERA5 grid points used to determine meteorological characteristics identified by red dots.

Rutz et al. 2015). Dunn (1983) identified a maximum in the frequency of high LPE snowfall events at Alta with west-northwest flow (~290°), with the heaviest events produced by northwest flow (310°–320°). He speculated that this was due to low-level convergence coupled with orographic lift and lake-effect storms. Northern Utah features a local maximum in strong cold-frontal passage frequency in the Intermountain West, as delineated by an abrupt temperature fall and pressure rise (Shafer and Steenburgh 2008). In some Wasatch storms, cold-frontal passages can feature an intrusion of low-θ_e air aloft, enabling heavy convective precipitation in the prefrontal phase (Steenburgh 2003). Cold-frontal passages can also be accompanied by heavy precipitation and be followed by postfrontal orographic and GSL-effect precipitation (Steenburgh 2003). Though it only represents about 5% of the total cool-season LPE in the central Wasatch, the GSL effect can produce heavy snowfall, especially in the early and latter parts of the cool season (Carpenter 1993; Steenburgh et al. 2000; Alcott et al. 2012; Alcott and Steenburgh 2013; Yeager et al. 2013). Prior research has linked inland-penetrating or decaying atmospheric rivers from the Pacific Ocean with orographic precipitation in the Wasatch, although they have not been examined systematically (Dettinger et al. 2011; Rutz and Steenburgh 2012; Rutz et al. 2014, 2015). Intermountain cyclones have also been tied to snowfall in the Wasatch (Zishka and Smith 1980; Whittaker and Horn 1981; Dunn 1983; Horel and Gibson 1994), often causing a decreased ratio of mountain to valley LPE (Williams and Peck 1962; Dunn 1983).

Although previous research has examined individual phenomena that contribute to extreme orographic snowfall in LCC, no studies have comprehensively analyzed the orographic snowfall characteristics and associated synoptic regimes. In this paper, we aim to fill this gap using modern reanalyses and radar observations. Additionally, most prior research on orographic precipitation has focused on extreme snowfall in the form of LPE, and as we will show here, the characteristics of extreme snow events differ somewhat from extreme LPE snowfall events since the former is also affected by the snow-to-liquid ratio (SLR). In section 2, we describe the data and methods used. In section 3, we present the seasonal and event characteristics of snowfall at a high-elevation observing site in upper LCC and discuss the flow dependencies, vapor-transport tendencies, synoptic environments, and radar characteristics associated with extreme snowfall events. Section 4 summarizes our results, which will aid forecasting, avalanche hazard assessment, and road-weather maintenance in Little Cottonwood Canyon and enhance knowledge of the mechanisms contributing to orographic precipitation extremes in mountainous regions.

2. Data and methods

a. Alta-Collins (CLN) snowfall observations

We used 12-h manual snow and LPE observations collected by the Alta Ski Patrol at their Alta-Collins (CLN) snow-study plot (2945 m MSL; see Fig. 1 for location) from the 2000 to 2022 cool seasons (year defined by the ending calendar year) to develop long-term statistics and identify snowfall extremes (Wasserstein and Steenburgh 2023). In the present climate, virtually all the cool-season precipitation at this altitude falls as snow. *Therefore, for the purposes of this analysis, "snow" represents the measured 12-h new-snow depth, "LPE" represents the water equivalent of that snow, and "snowfall" represents precipitation falling in the form of snow*. The snow and LPE measurements were collected in a forested clearing on a standard snowboard placed on the existing snowpack at 0400 and 1600 LST, with LPE obtained with a Snowmetrics sampling tube and scale since at least 2002 (prior sampling method unknown). Alcott and Steenburgh (2010) used 24-h measurements from this location to examine snow-to-liquid ratio at Alta, but we use 12-h observations here since the higher-frequency measurements are now being provided by Alta Ski Patrol and there is less evolution in the synoptic conditions during the shorter period. Although recorded in inches and hundredths of an inch, throughout this paper, we use units of centimeters and millimeters for snow and LPE, respectively. We quality controlled the data through comparison with precipitation and snow observations at the nearby Alta National Weather Service COOP site (2655 m MSL) and the Utah Department of Transportation Alta Guard Station (2682 m MSL) and by examining synoptic reanalyses during precipitation periods. There were four measurements that we deemed questionable, and we either adjusted the date and time to match nearby observations and reanalysis data or eliminated the observation entirely (Table 1). Each questionable event occurred in October, before Alta Ski Area opened for the season, which may have contributed to a mislabeling of an observation date or measurement.

TABLE 1. Adjustments made to CLN snow and LPE observations.

Original event end time (LST)	New event end time (LST)
0400 LST 17 Oct 2004	Removed from analysis
0400 LST 23 Oct 2004	0400 LST 24 Oct 2004
1600 LST 30 Oct 2004	1600 LST 31 Oct 2004
0400 LST 27 Oct 2010	1600 LST 27 Oct 2010

We defined 12-h periods with ≥2.54 cm of snow as a "snow event" and ≥2.54 mm of LPE as an "LPE event." These thresholds eliminate the lowest snow and LPE observations in the dataset, with the former being the minimum recorded snowfall amount for a majority of the observational period (i.e., since 2002) and reliable manual measurement of the latter being difficult when snowfall or LPE is low. We identified the 95th percentile of snow or LPE during these events and classified each as a "snow extreme" or an "LPE extreme." Thus, these are 12-h extremes rather than 24-h or multiday events. Tables A1 and A2 in the online supplemental material list the dates of each snow and LPE extreme and important variables for this study associated with each extreme. Although 26 (19%) of the snow and 30 (26%) of the LPE extremes occurred during consecutive 12-h periods that last either 24 or 36 h, we treat each as its own event in this paper since removing all but one 12-h period in each of the consecutive periods did not change the results.

b. ERA5 reanalysis

To examine the meteorological conditions associated with orographic snowfall at CLN, we used the European Centre for Medium-Range Weather Forecasts Reanalysis v5 (ERA5; Hersbach et al. 2020). The ERA5 contains global meteorological variables on a 0.25° grid at hourly intervals on pressure levels ranging from 1000 to 1 hPa. There are four ERA5 grid points that surround the central Wasatch (see Fig. 1 for locations), and we averaged data over those four grid points to classify the local meteorological conditions at the midpoint of each 12-h observation period. Sensitivity testing revealed that using the start time, end time, or time average for the 12-h period did not substantially impact results. We binned all events into 1 of 16 wind directions (e.g., north, north-northeast, northeast) using the 700-hPa (the closest mandatory pressure level to crest level) wind direction.

c. KMTX radar

To examine the characteristics of mesoscale precipitation features during orographic snowfall extremes at CLN, we used level II data (NOAA National Weather Service 1991) from the Salt Lake City, Utah (KMTX), WSR-88D radar located at 2000 m MSL on Promontory Point above the Great Salt Lake (Fig. 1b). We focus on events beginning with the 2009 cool season when the resolution of the radar data increased to superresolution. For LPE extremes, none of the 75 events that occurred during or after the 2009 cool season had missing radar data, and for snow extremes, data were missing for only one of the 83 events (1.2%). To study the spatial distribution of precipitation, we examined the frequency of radar echoes $\geq$ 10 dBZ for all available 0.5° radar scans during events. We used 10 dBZ because it represents an approximate threshold for accumulating snowfall and has been used in prior studies in northern Utah (e.g., Steenburgh et al. 2000; Yeager et al. 2013). KMTX often experiences beam blockage by the Wasatch Range, and the 0.5° scan can overshoot or undersample shallow orographic convection, reducing the accuracy of quantitative precipitation estimates at specific locations (Wood et al. 2003). Thus, we use a fixed dBZ threshold, rather than an LPE estimate, to characterize the spatial precipitation patterns associated with snowfall.

d. Synoptic classifications

We manually classified all snow and LPE extremes into one of eight synoptic classifications that we identified using ERA5 analyses of 500-hPa geopotential height and absolute vorticity, sea level pressure, 700-hPa temperature, 700-hPa relative humidity, 700-hPa wind, and vertically integrated water vapor transport (IVT) magnitude and vectors at the midpoint of each event. Radar imagery was sometimes consulted to ascertain the nature of precipitation features (e.g., frontal and postfrontal convection). We calculated IVT from the ERA5 surface to 300 hPa using

$$\mathrm{IVT} = \sqrt{\left(\frac{1}{g}\int_{\mathrm{sfc}}^{300} qu\,dp\right)^2 + \left(\frac{1}{g}\int_{\mathrm{sfc}}^{300} qv\,dp\right)^2}, \qquad (1)$$

where q is the specific humidity (kg kg^{-1}), u and v are the zonal and meridional winds (m s^{-1}), p is the pressure (Pa), and g is the acceleration due to gravity. We used eight synoptic classifications: southerly IVT (SIVT), southwesterly IVT (SWIVT), westerly IVT (WIVT), northwesterly IVT (NWIVT), post-cold-frontal northwesterly flow (NW Postfrontal), cold-fronts or baroclinic troughs (Frontal), south-southwesterly cold core flow (SW Cold Core), and closed low pressure systems (Closed Low). The IVT events were associated with elevated IVT, typically extending toward the central Wasatch from the classification direction, with mean IVT over the central Wasatch $\geq$ 100 kg m^{-1} s^{-1}. These events featured elongated corridors of elevated IVT, but magnitudes over the central Wasatch may be below the commonly used threshold for an atmospheric river (250 kg m^{-1} s^{-1}) due to declining IVT with inland penetration (Rutz et al. 2014, 2015). The classification direction was based on the ERA5 700-hPa wind direction (i.e., 157.5°–202.5°, 202.5°–247.5°, 247.5°–292.5°, and 292.5°–332.5° for the SIVT, SWIVT, WIVT, and NWIVT events, respectively), which approximates the crest-level water vapor transport direction and is often used by local forecasters to anticipate local orographic precipitation enhancement. Results based on IVT direction were comparable. Two events with a weak short-wave trough embedded in large-scale westerly flow fell in the SWIVT classification based on these objective criteria. We modified these events to WIVT as that was the predominate large-scale flow direction. The NW Postfrontal events featured northwesterly 700-hPa flow in the wake of a 700-hPa front or trough with the central Wasatch experiencing cold or weak advection. Frontal events were associated with a cold front, quasi-stationary front, or baroclinic trough and associated precipitation band. Some Frontal events had mean IVT over the central Wasatch $\geq$ 100 kg m^{-1} s^{-1}, meeting the minimum criteria for classification as an IVT event, but their frontal characteristics distinguish them from events in the IVT classifications. The SW Cold Core events were produced by a deep upper-level trough over the southwest United States with the central Wasatch in cold core south-southwesterly flow. These events also featured lower IVT (i.e., $<$100 kg m^{-1} s^{-1}). Last, events with closed 700-hPa circulation near or over northern Utah with the central Wasatch in the frontal baroclinity or thermal warm tongue just ahead of the low center fell in the Closed Low classification. We labeled events that did not clearly fit in any one of those eight classifications as not applicable (N.A.). These events could have featured the following: 1) IVT $<$ 100 kg m^{-1} s^{-1}, failing to meet the criteria for an IVT event, 2) elements of multiple classifications, 3) synoptic frontal characteristics (e.g., wind shift and baroclinity), but either radar data were not available to confirm the presence of a frontal precipitation band or such a band was not evident in radar, or 4) characteristics that did not fit any of the eight categories.

3. Results

a. Event and seasonal snowfall characteristics

We begin with an examination of event, monthly, and seasonal snow and LPE characteristics at CLN in upper LCC. We identified 2707 snow events over the 23-yr period, with a mean and median of 11.2 and 7.6 cm, respectively (Fig. 2a). As

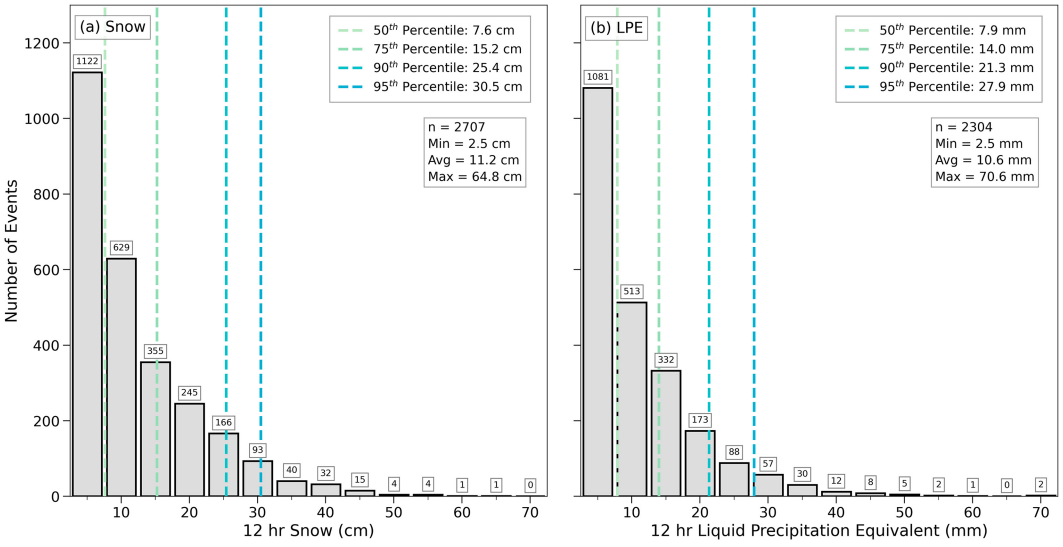

FIG. 2. Histograms of 12-h (a) snow and (b) LPE events at CLN during the 2000–22 cool seasons. Bins in (a) are in 5-cm increments starting at 2.5 cm, and in (b), they are in 5-mm increments starting at 2.5 mm. Dashed vertical lines indicate the 50th, 75th, 90th, and 95th percentiles. The number of events in each bin is annotated at the top of bars.

is often the case with precipitation (e.g., Martinez-Villalobos and Neelin 2019), the event-size frequency exhibited a gamma distribution with over 1700 events < 12.5 cm, 10 events ≥ 48.5 cm, and a maximum of 64.8 cm. There were 138 95th percentile snow extremes with $\geq$30.5 cm of snow. For LPE, we identified 2304 events with a mean and median of 10.6 and 7.9 mm, respectively (Fig. 2b). The event-size distribution was similar to snow with an abundance of small events, 10 events $\geq$ 48.5 mm, and a maximum of 70.6 mm. There were 116 95th percentile LPE extremes with $\geq$27.9 mm of LPE. Only 52 events met *both* the extreme snow and LPE thresholds.

Featuring a transitional (a.k.a. intermountain) snow climate, the central Wasatch observes high seasonal snow and moderate wintertime temperatures with elements of continental or coastal snow climates depending on the season (Whiteman 2000; Mock and Birkeland 2000). During the 23-season study period, seasonal snow at CLN ranged from 831.9 to 1877.1 cm and LPE ranged from 726.4 to 1681.7 mm, with means of 1340.4 cm and 1116.9 mm, respectively (Fig. 3). The 2011 cool season produced the most snow (181) and LPE (196) events, whereas the 2015 cool season saw the fewest snow (96) and LPE (109) events. Median monthly snow and LPE increased from October to December, consistent with the transition to the cool season (Fig. 4). Median monthly snow and LPE from December to April are ~200 cm and ~175 mm, respectively, and although there are variations from month to month, the differences are not statistically significant at the 95th percent confidence interval (hereinafter, statements of significance are based on a 95th percent confidence interval).

Indicative of the large variety of storm tracks and types that produce orographic snowfall extremes in the central Wasatch, there is a wide range of SLRs in individual 12-h periods at CLN. We generated SLR statistics for the 1903 events with $\geq$5.1 cm of snow and $\geq$2.8 mm of LPE in the 23-season study period. These criteria reduce relative errors in SLR due to rounding and measurement (Judson and Doesken 2000; Roebber et al. 2003; Baxter et al. 2005). The snow-to-liquid ratio in these periods ranged from 1.6 to 50, with a mean of 13.8 and a median of 12.8 (Fig. 5), comparable to results from Alcott and Steenburgh (2013), who found a mean of 14.4 and a median of 13.3 at CLN for November–April 1999–2007. Our lower values are likely due to our inclusion of October in our analysis and the different study period that includes observations through 2022.

El Niño–Southern Oscillation (ENSO) is an important driver of weather and climate variability in the continental western United States (Bjerknes 1966, 1969; Rowntree 1972; Horel and Wallace 1981; Ropelewski and Halpert 1986; Trenberth et al. 1998). Although the ENSO phase can have seasonal precipitation impacts on regions in the American West [e.g., positive ENSO has links to increased precipitation in California (Cayan et al. 1999; Jong et al. 2016) and negative ENSO has links to increased precipitation in the Pacific Northwest (Redmond and Koch 1991)], northern Utah's mountains fall at the nodal point in the ENSO dipole where the ENSO phase has little correlation with seasonal precipitation trends (Redmond and Koch 1991). Using snow and LPE data at CLN and the multivariate ENSO index version 2 (MEI.v2; available at https://psl.noaa.gov/enso/mei; Wolter and Timlin 2011), we analyzed the relationship between the ENSO index and 2-month accumulated snow (Fig. 6a) and LPE (Fig. 6b). Consistent with prior research, ENSO has no discernable relationship with observed snow or LPE at CLN. In any 2-month subseasonal period, strong positive ENSO periods (i.e., ENSO index $\geq$ 1.5) and strong negative ENSO periods (i.e., ENSO index ≤ -1.5) do not consistently produce more or less snow or LPE at CLN than neutral phases or weak periods. The Pearson correlation coefficients between the 2-month ENSO index and snow and LPE were -0.03 and -0.01, respectively, indicative of the

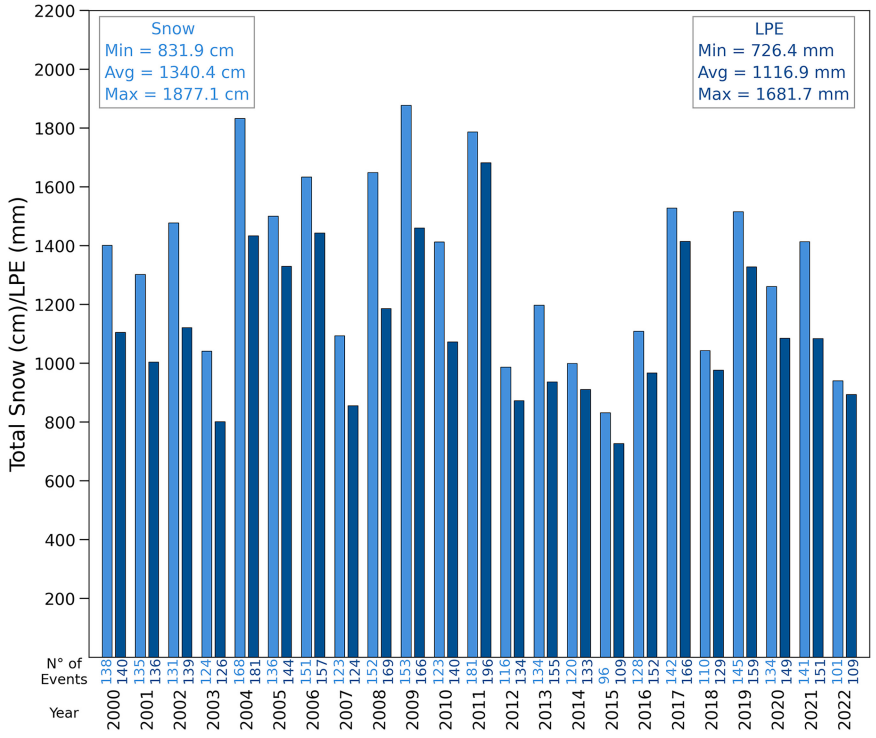

FIG. 3. Total seasonal snow (cm; light blue) and LPE (mm; dark blue) during the 2000–22 cool seasons. The number of events during each season is annotated at the bottom of bars.

lack of relationship between ENSO and snowfall in the central Wasatch.

b. *Flow dependencies*

We now examine the relationship between the 700-hPa (near crest level) flow and orographic snowfall extremes at CLN. For context, the cool-season climatological 700-hPa wind directions are most frequently southerly to northwesterly with wind speeds of 5–10 m s^{-1} (Fig. 7a). There is weak bimodality in the wind direction frequency with maxima from the west-northwest and south-southwest. Higher wind speeds are also more frequent from these flow directions. A similar

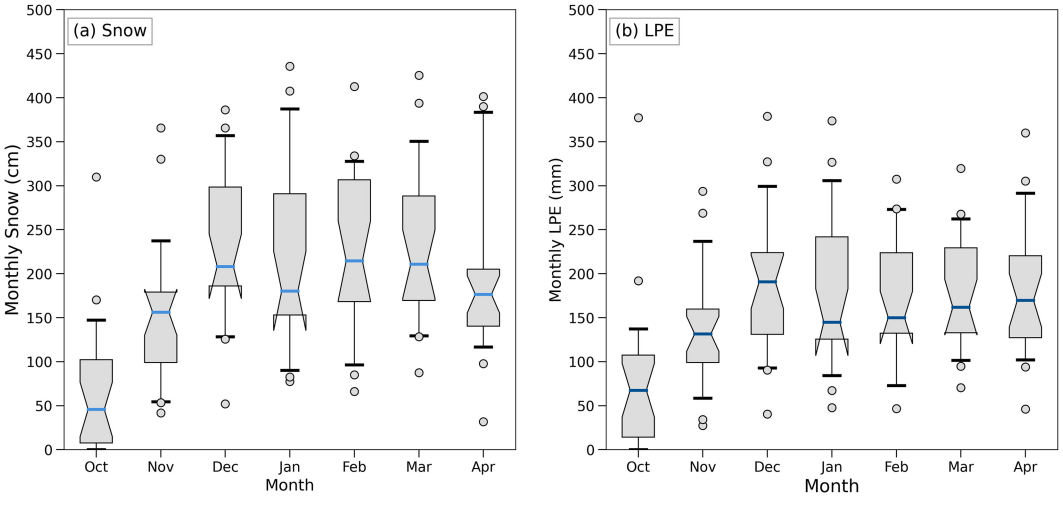

FIG. 4. Box-and-whisker plots of monthly (a) snow and (b) LPE at CLN during the 2000–22 cool seasons. The colored horizontal line represents the median, the box represents the 25–75th percentile, the whiskers represent the 5th and 95th percentiles, and the circles represent outliers. Notches indicate the 95% confidence interval of the median as computed using Gaussian-based asymptotic approximation.

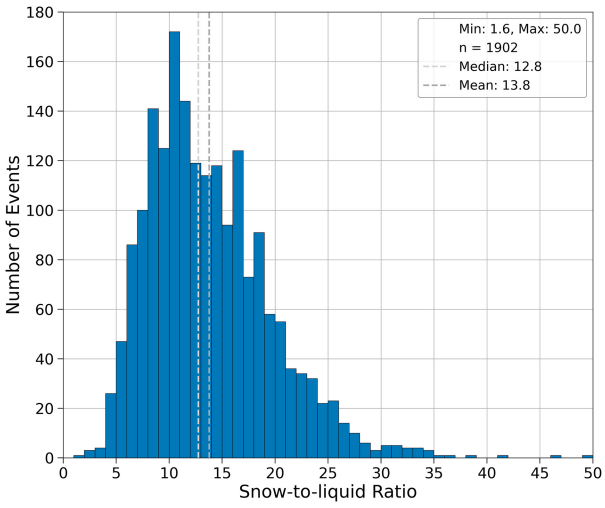

FIG. 5. Histogram of snow-to-liquid ratio for all events at CLN with ≥5.1 cm of snow and ≥2.8 mm of LPE. Bins have a width of 1. Light and dark gray lines indicate the median and mean, respectively.

distribution exists for all snow and LPE events, although the bimodality strengthens and west-northwesterly flow emerges as the primary maximum (Figs. 7b,c). This indicates a greater likelihood of snowfall during west-northwesterly flow than other flow directions. For snow extremes, the west-northwesterly flow maximum strengthens further, although such events occur for a wide range of flow directions and there is a weak secondary maximum for west-southwesterly flow (Fig. 7d). To illustrate the primacy of the west-northwesterly flow snow maximum, 80 (58.0%) of the 138 snow extremes featured west to northwest flow and 44 (31.9%) specifically featured from the west-northwest (percentages not shown explicitly in Fig. 7). In contrast, extreme LPE events feature stronger bimodality and a less prominent west-northwesterly flow maximum (Fig. 7e). Additionally, wind speeds are higher for LPE extremes than for snow extremes.

The bimodal relationship of LPE extremes to wind direction contrasts with the modal distributions identified for major precipitation events in the Sierra Nevada (e.g., Pandey et al. 1999; see their Fig. 5) and Cascade Range near Portland, Oregon (e.g., Yuter et al. 2011; see their Fig. 2), where the flow interacts with broad, quasi-linear mountain barriers. We hypothesize that the bimodality at CLN reflects three characteristics of the regional terrain and geography. The first is the presence of the Oquirrh Range to the west of the central Wasatch, which lies on a bearing from ~235° to 290° relative to CLN and potentially contributes to a decline in event frequencies in southwest to westerly flow. The Stansbury Range farther upstream could also contribute to this event frequency decline. In addition, during northwesterly flow, blocking by the Oquirrh Range has been shown to enhance convergence and precipitation produced upstream of the central Wasatch over the Salt Lake Valley (Alcott and Steenburgh 2013), potentially contributing to an increase in event frequencies from that flow direction. The second is the broader, three-dimensional topography of the central Wasatch, which includes zonally oriented subbarrier ridges that are the highest local terrain features and oriented nearly orthogonal to the otherwise quasi-meridional Wasatch Range. As a result, instead of a single optimal flow direction for upslope flow as occurs over a linear barrier, flow from multiple directions is potentially forced over the central Wasatch, especially the high terrain surrounding Little Cottonwood Canyon. The third is the Great Salt Lake, which contributes to lake-effect storms and approximately 5% of the cool-season precipitation in upper Little Cottonwood Canyon during northwesterly flow (Alcott et al. 2012; Yeager et al. 2013).

The more pronounced west-northwesterly flow maximum for snow extremes compared to LPE extremes reflects the compounding influence of SLR, which exhibits considerable variability at CLN (e.g., Fig. 5) and inversely correlates strongly with the near-crest-level temperature (Alcott and Steenburgh 2010). Thus, while LPE extremes may be favored by higher temperatures when the absolute humidity is higher,

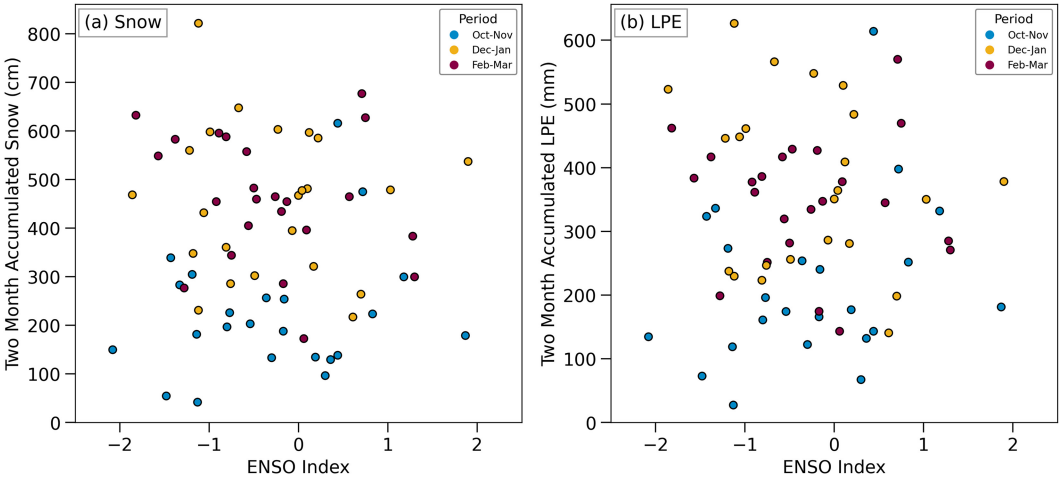

FIG. 6. Scatterplot of ENSO index and (a) 2-month accumulated snow and (b) 2-month accumulated LPE at CLN.

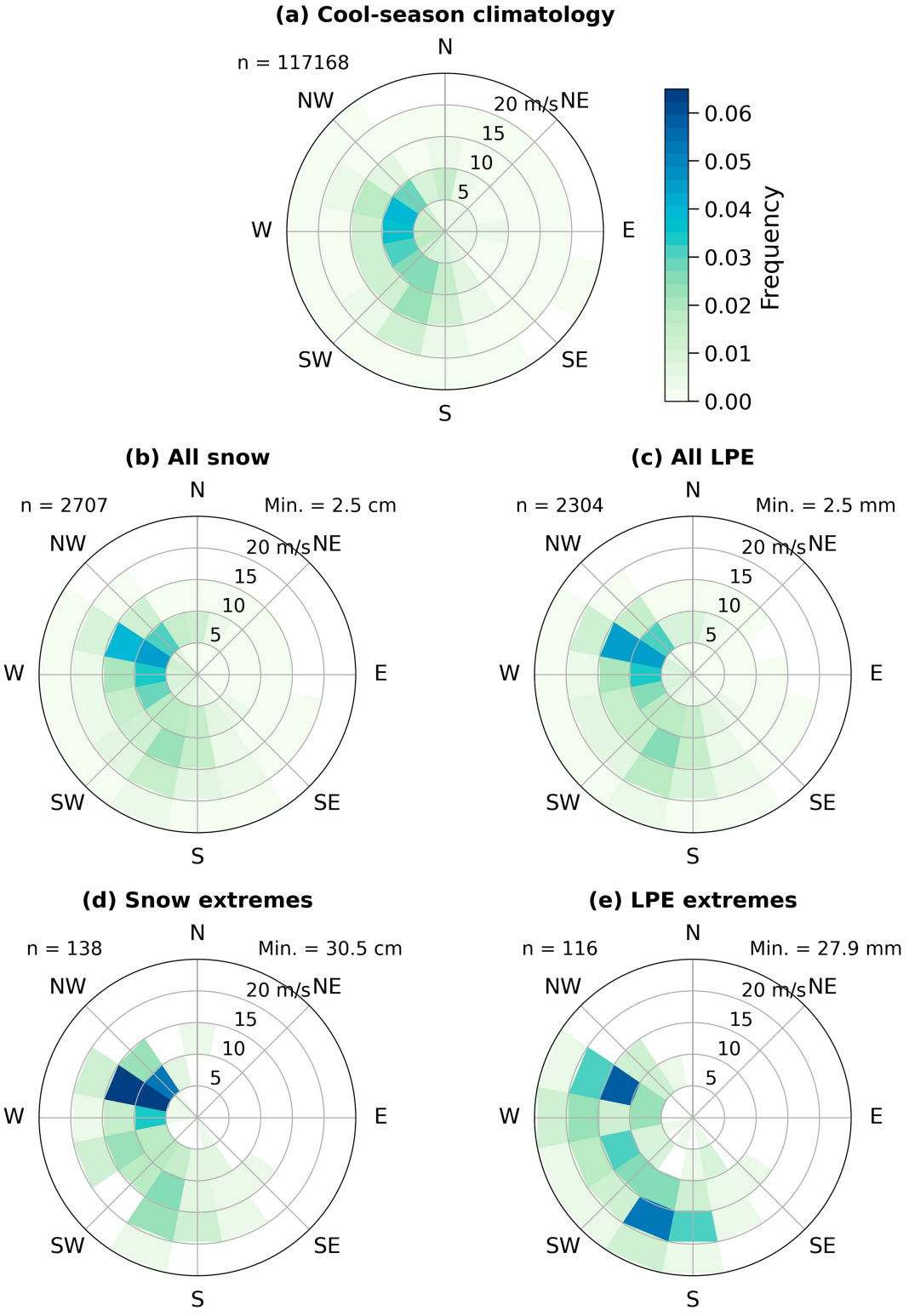

FIG. 7. Normalized polar histograms of 700-hPa wind speed and direction frequency in the central Wasatch. Bins are in 5 m s^{-1} and 22.5° increments. (a) Cool-season climatology. (b)–(e) As in (a), but for all snow events, all LPE events, snow extremes, and LPE extremes, respectively.

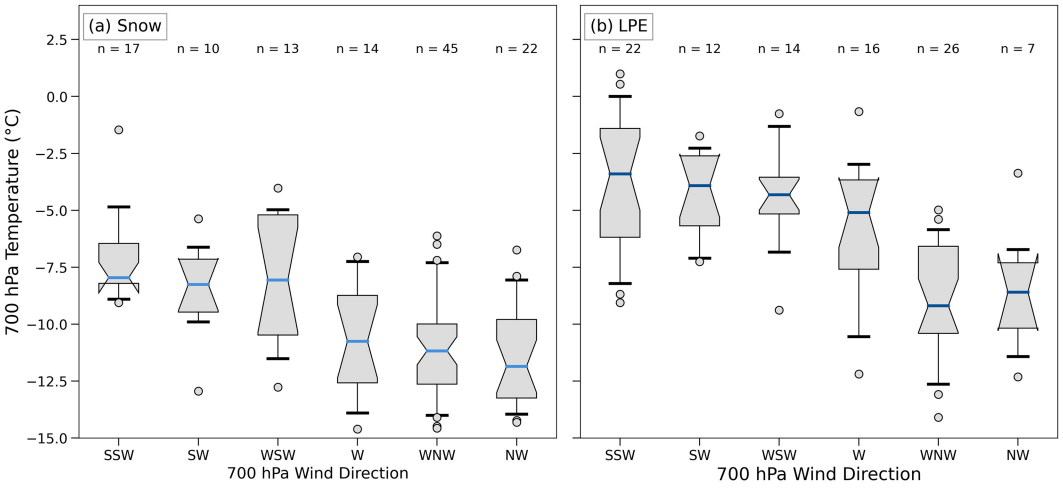

FIG. 8. Box-and-whisker plots of 700-hPa temperatures for (a) snow and (b) LPE extremes binned by 700-hPa wind direction. Convention same as Fig. 4.

snow extremes can occur at lower temperatures when the SLR is large. Indeed, a comparison of the 700-hPa temperatures during snow and LPE extremes shows that the former are substantially colder, with the medians 2.0°–5.9°C lower depending on the 700-hPa wind direction (cf. Figs. 8a,b). Given the inverse correlation of SLR with near-crest-level temperatures, this leads to substantially higher SLRs in snow extremes than in LPE extremes (cf. Figs. 9a,b). The pronounced west-northwesterly–northwesterly flow maximum for snow extremes is consistent with such flow directions favoring colder temperatures and higher SLR snowfalls.

An important question concerns the representativeness of the midpoint wind direction in each 12-h period. To examine this, we produced polar histograms of the ERA5 700-hPa wind direction at *each hour* during LPE extremes for each midpoint 700-hPa wind direction (Fig. 12). For brevity, we focus on south-southwest, southwest, west-southwest, west, west-northwest, and northwest midpoint wind directions because they comprise the bulk of the LPE extremes. Most LPE extremes have little wind direction variability, with the midpoint wind direction being the mode and relatively high frequencies occurring in adjacent direction bins (Fig. 10). Variability, as indicated by a broader wind-direction distribution, was greatest for southwesterly, west-southwesterly, and westerly events, which likely reflects a high frequency of trough passages (Figs. 10b–d). Conversely, events with south-southwesterly, west-northwesterly, and northwesterly flow have greater flow persistence, consistent with a sharper peak at or near those flow directions (Figs. 10a,e,f). We obtained similar results for snow extremes (not shown).

c. *Synoptic classifications of extreme events*

As discussed in section 2d, our manual classification of snow and LPE extremes revealed eight patterns that generate extreme orographic snowfall at CLN (SIVT, SWIVT, WIVT,

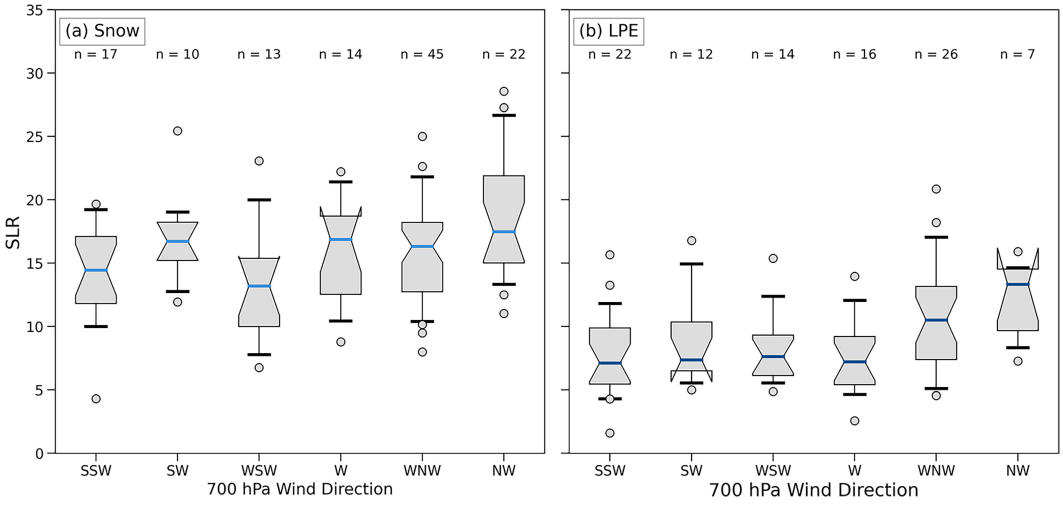

FIG. 9. As in Fig. 8, but for SLR.

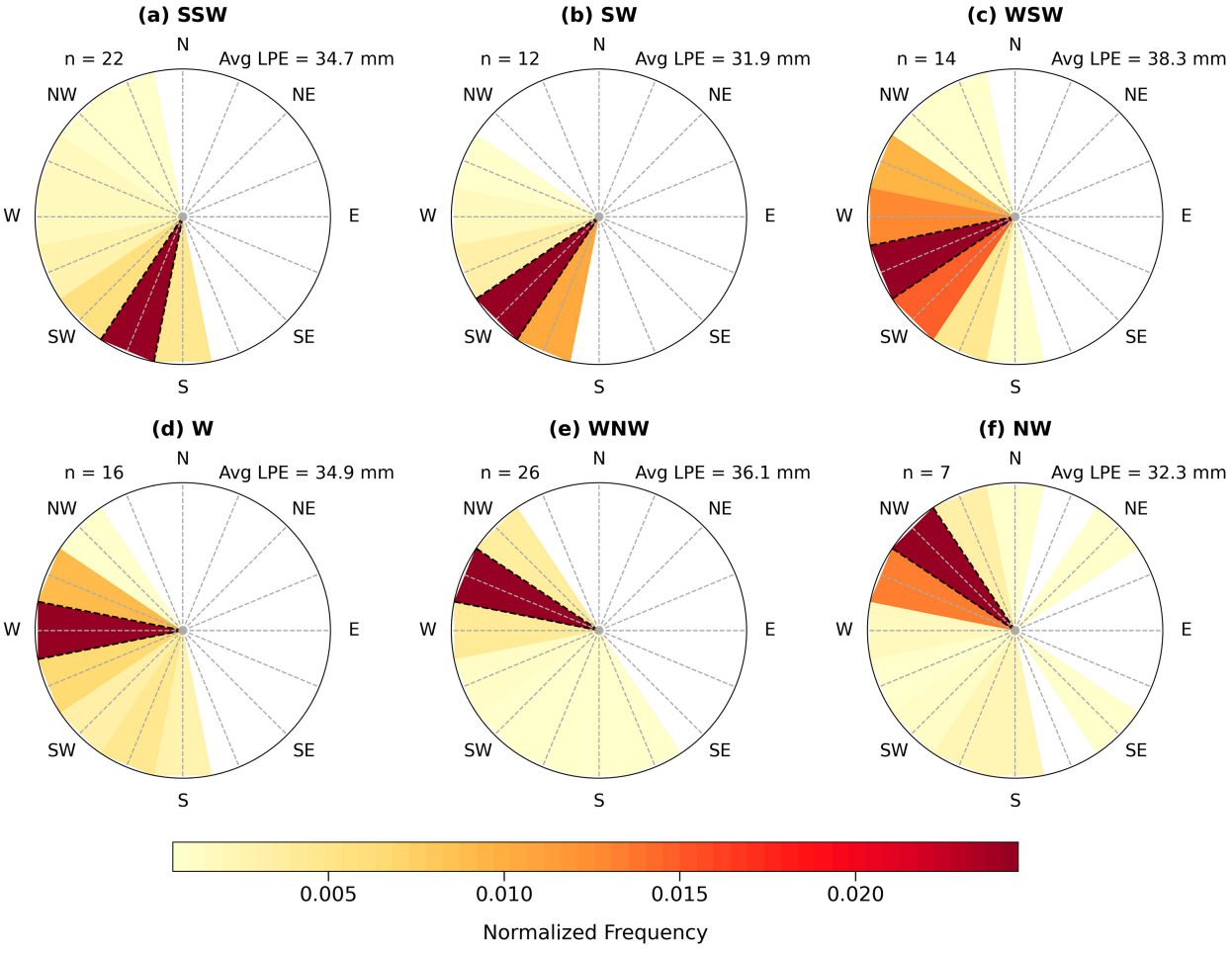

FIG. 10. Normalized frequency of 700-hPa wind direction during each LPE extreme binned by wind direction classification (color bar at bottom). The number of events is listed in the top-left corner. (a) South-southwesterly flow. (b)–(f) As in (a), but for southwesterly, west-southwesterly, westerly, west-northwesterly, and northwesterly flow, respectively.

NWIVT, NW Postfrontal, Frontal, SW Cold Core, and Closed Low). Just under 40% of the LPE extremes fell into one of the high IVT classifications, with SWIVT the most common (Fig. 11). This fraction is much higher than for snow extremes (8%, Fig. 11), likely because high IVT events are often warmer, have lower SLRs, and are less likely to generate snowfall extremes. In contrast, nearly 50% of the snow extremes were NW Postfrontal, compared to only 18% of LPE extremes, which likely reflects the tendency for such events to feature high SLRs and generate large snowfalls from low to moderate LPE. Frontal was the most common LPE classification and the second most common snow classification. For both snow and LPE extremes, SW Cold Core and Closed Low made up less than 10% of events. While these eight synoptic classifications represent the majority of central Wasatch snowstorms, there were some snow and LPE extremes which did not fall clearly into any one of the eight synoptic classifications, and we labeled these events as N.A. (Fig. 11).

We produced composites of IVT, 500-hPa geopotential height, and 700-hPa temperature and winds for each synoptic type for both snow and LPE extremes. For brevity, we show only the latter since the snow extreme composites were qualitatively similar. Because there were only three LPE extremes that we classified as Closed Low, we omitted Closed Low events from this composite analysis. For each high IVT synoptic type, IVT penetration into the interior occurs to the north or south of the high Sierra Nevada (hereinafter high Sierra) south of Lake Tahoe (Figs. 12a–d). For the SIVT and SWIVT composites, the high IVT values circumscribe the southern high Sierra and penetrate into northern Utah via the lower Colorado River Basin (Figs. 12a,b). For the WIVT composite, high IVT values extend across the northern Sierra and southern Cascades to northern Utah (Fig. 12c). These results are consistent with Rutz et al. (2014, 2015) who showed that the high Sierra south of Lake Tahoe contribute strongly to declining IVT and atmospheric river (AR) decay due to water vapor depletion by orographic precipitation. Finally, for the NWIVT composite, the high IVT values move across the Cascade Range and then over the low-elevation Snake River Plain to northern Utah (Fig. 12d). In each high IVT composite, 700-hPa

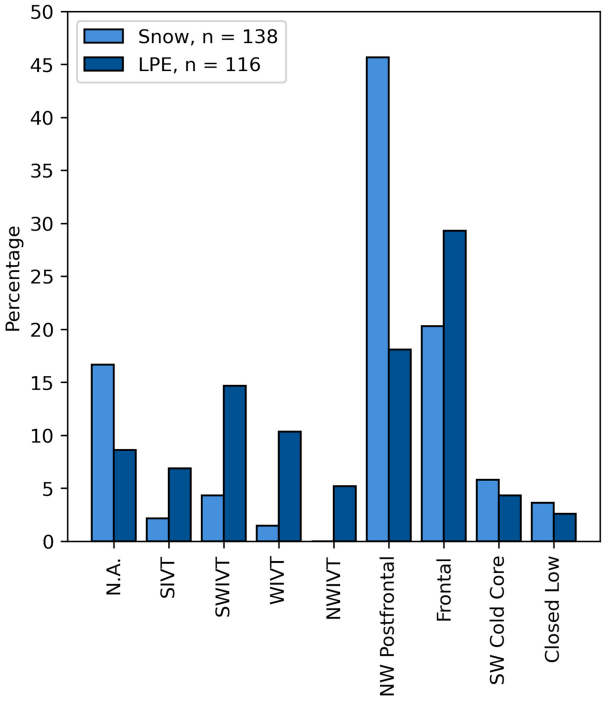

FIG. 11. Percentage of snow and LPE extremes by synoptic classification.

winds over the central Wasatch are ~15 m s^{-1}, stronger than the modal wind speeds at this level, which are 5–10 m s^{-1} (see Fig. 7a). Composite 700-hPa temperatures in the central Wasatch are near −3°C for SIVT, SWIVT, and WIVT and −5°C for the NWIVT composite (Figs. 12a–d). These are relatively high temperatures for cool-season storms at CLN (see Fig. 8). The strong flow and high temperatures in these high IVT events often result in high LPE but modest snowfall totals. For each composite, the mean SLR is less than 9, substantially less than the mean SLR at CLN of 13.8 (Fig. 5), but comparable with typical SLR values during LPE extremes (Fig. 9b).

Although over a third of the LPE extremes fall into one of the high IVT synoptic types, orographic storms in the central Wasatch often occur in synoptic environments not associated with high IVT. NW Postfrontal LPE storms are substantially colder than the high IVT synoptic types, with composite 700-hPa temperatures near −9°C (Fig. 13a); additionally, IVT values are much lower, with composite values from 50 to 100 kg m^{-1} s^{-1} over the central Wasatch (Fig. 13a). This synoptic classification also has weaker winds that are closer to the climatological wind speed frequency maximum for west-northwest and northwest flow (see Fig. 7a). As evidenced by the tight packing of 700-hPa temperature contours in Arizona and New Mexico (downstream of Utah), the environment is clearly postfrontal (Fig. 13a). Given the cold nature of NW Postfrontal storms (Figs. 9 and 13a), the mean SLR for these events is 11.5, higher than the SLR values for the high IVT synoptic types and close to median (see also Fig. 8a). For snow extremes in the NW Postfrontal classification (composite not shown), the mean SLR is 17.4, well above median. During Frontal events, a distinct 700-hPa wind shift from southwesterly to northwesterly coincident with a baroclinic zone over northern Utah is indicative of a frontal trough moving through the region (Fig. 13b). These events can be associated with mobile cold-frontal or quasi-stationary frontal bands. Last, SW Cold Core events had a deep upper-level trough over the southwest and IVT < 100 kg m^{-1} s^{-1} in the cold core south-southwesterly flow with 700-hPa temperatures ~−7°C in the central Wasatch (Fig. 13c). The cold nature of these events yielded a mean SLR of 11.9, higher than the mean SLR for high-IVT events with southerly or southwesterly flow.

d. *Vapor transport diagnostics and Local Precipitation Efficiency*

Extreme orographic precipitation in some mountainous regions is closely related to high IVT directed toward the orography (e.g., Ralph et al. 2006; Neiman et al. 2011; Rutz et al. 2014; Froidevaux and Martius 2016; Lorente-Plazas et al. 2018; Ralph et al. 2019). Here, we present the relationships between time-integrated IVT (TIVT) and snow and LPE extremes in the central Wasatch, calculating TIVT as follows:

$$\mathrm{TIVT} = \int_{t_i}^{t_f} \mathrm{IVT}\,dt, \tag{2}$$

where t_i and t_f are the initial and final times in a 12-h observation period, respectively. For comparison purposes, a constant IVT of 250 kg m^{-1} s^{-1} over 12 h yields a TIVT of 1.08×10^7 kg m^{-1}. Snow extremes have relatively low TIVT compared to LPE extremes, with values $\leq 0.6 \times 10^7$ kg m^{-1} for all but five events (cf. Figs. 14a,b). Snow events are most frequently NW Postfrontal, which feature relatively low TIVT, as evidenced by the tight clustering of orange points with northwesterly crest-level flow in Fig. 14a. The five rare high TIVT snow events occurred in southerly to westerly flow (Fig. 14a).

LPE extremes in the central Wasatch skew toward higher TIVT compared to extreme snow events, with about half featuring TIVT $\geq 0.6 \times 10^7$ kg m^{-1} and many falling in one of the four high IVT synoptic classifications (Fig. 14b). Despite low TIVT, the NW Postfrontal synoptic classification produced several LPE extremes, illustrating the relatively efficient conversion of water vapor to precipitation by postfrontal orographic convection or the influence of the GSL effect. One NW Postfrontal event, for instance, was one of the ten largest LPE events and had TIVT ~ 0.2×10^7 kg m^{-1} (Fig. 14b). Similar to the low TIVT environments associated with post-cold-frontal northwesterly flow, SW Cold Core events have low TIVT, but feature southerly to southwesterly flow (Fig. 14b). The efficient conversion of water vapor to precipitation in these events occurs within the unstable cold core of the upper level low where orographic convection is common. Part of the reason why only 52 of the snow and LPE extremes are the same event is that the two types of extremes are so distinct. While snow events tend to feature low TIVT and high snow-to-liquid ratios under west-northwesterly–northwesterly flow, LPE extremes are often associated with high TIVT and low snow-to-liquid ratios.

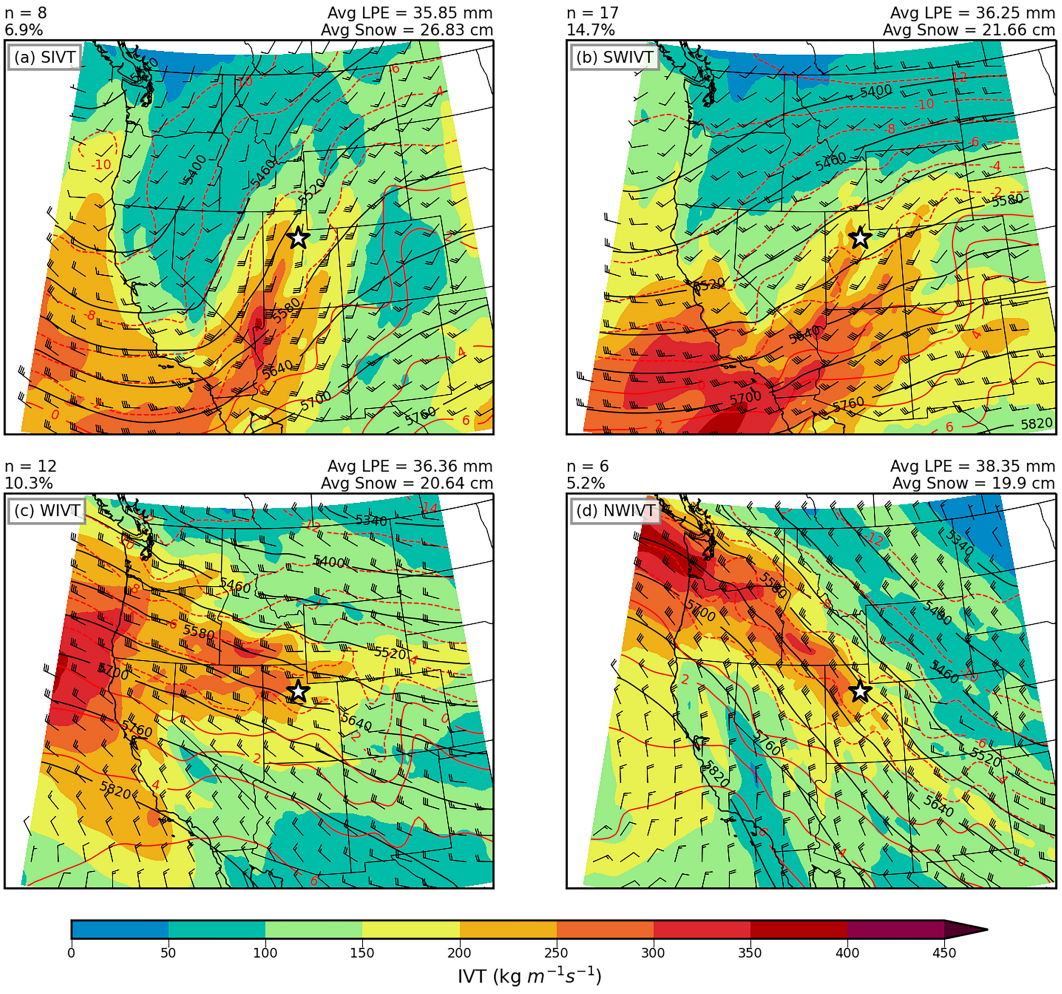

FIG. 12. Composites of IVT (kg m^{-1} s^{-1}; color-fill scale at bottom), 500-hPa geopotential height (m; black contours), 700-hPa temperature (°C; red contours), and 700-hPa wind (barbs; full barb = 5 m s^{-1}) for (a) SIVT, (b) SWIVT, (c) WIVT, and (d) NWIVT LPE extremes. The number of events and percentage of all LPE extremes are annotated at the top left. Average LPE and snow are annotated at upper right. The star indicates the location of the study domain.

To further examine the efficiency of water vapor conversion to precipitation, we define the Local Precipitation Efficiency as the ratio of LPE to TIVT:

$$\text{Local Precipitation Efficiency} = \frac{\text{LPE}}{\text{TIVT}}. \quad (3)$$

This ratio is equivalent to the drying ratio that has been used to quantify airmass transformation over mountain barriers (e.g., Smith et al. 2003; Kirshbaum and Smith 2008; Eidhammer et al. 2018) except that the control volume encloses a unit surface area (i.e., 1 m^2) rather than an entire mountain barrier. Due to this difference in volume, Local Precipitation Efficiency magnitudes are several orders of magnitude smaller than mountain-barrier drying ratios. We use the phrase "Local Precipitation Efficiency" because our focus here is on the local conversion of water vapor flux to precipitation rather than the airmass transformation across a mountain barrier. Similarly, Eidhammer et al. (2018) used precipitation efficiency synonymously with the drying ratio for mountain ranges in Colorado. We note, however, that this precipitation efficiency definition is not equivalent to other precipitation efficiency definitions such as the ratio of precipitation to condensate [i.e., the fraction of condensate that reaches the ground as precipitation (e.g., Kirshbaum and Smith 2008; Narsey et al. 2019)], the ratio of precipitation to the sum of vapor convergence and surface evaporation (e.g., Sui et al. 2007), or the ratio of precipitation to integrated water vapor (Bordi et al. 2016).

For snow and LPE extremes, the median Local Precipitation Efficiency is highest when the 700-hPa flow direction is west-northwesterly or northwesterly (Figs. 15a,b). Many of these periods feature postfrontal orographic or GSL-effect convection that efficiently generates snowfall despite low TIVT (Figs. 15a,b). The difference in median Local Precipitation Efficiency between

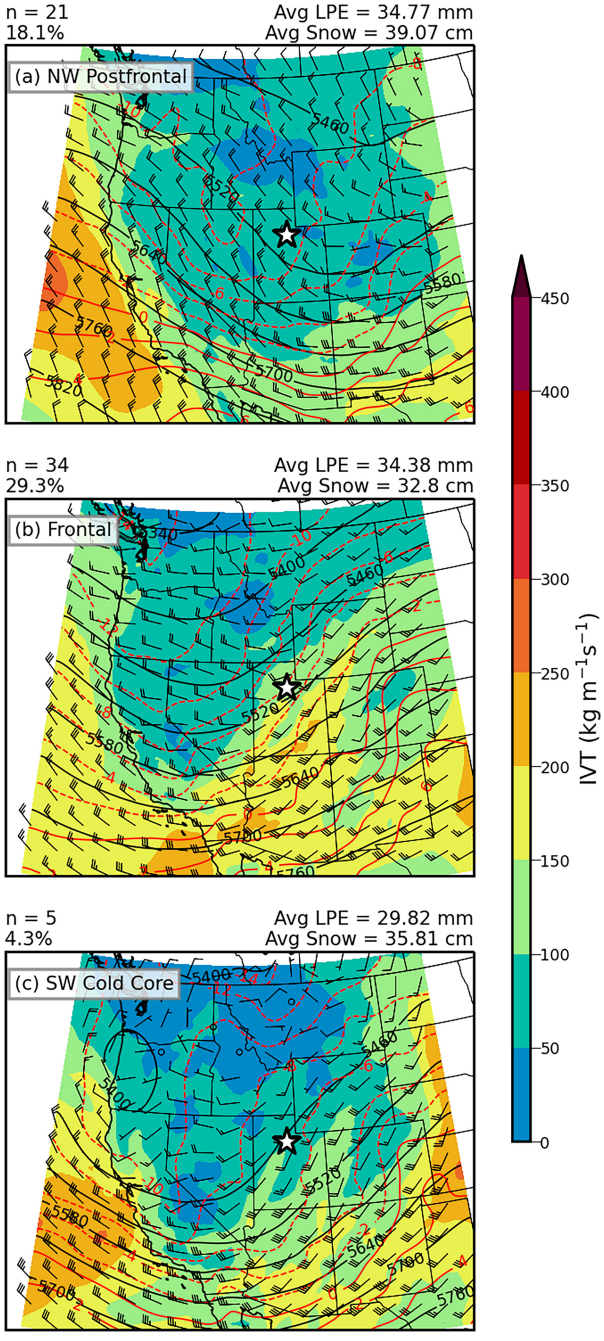

FIG. 13. As in Fig. 12, but for (a) NW Postfrontal, (b) Frontal, and (C) SW Cold Core LPE extremes.

west-northwesterly or northwesterly flow and all other directions except westerly is statistically significant for both snow and LPE extremes. For LPE extremes, the difference is also significant for westerly flow. The two outlier events in west-northwesterly and northwesterly flow with Local Precipitation Efficiency $> 3.5 \times 10^{-5}$ occurred during a lake-effect storm in October 2010. Such lake influences are not resolved by the ERA5 and serve as a nonorographic precipitation forcing mechanism that is not adequately accounted for by TIVT, which is more applicable to orographic precipitation.

e. *Relationship between high IVT and LPE*

The above results and prior research (e.g., Rutz et al. 2014; their Fig. 2a) indicate limited linkages and relatively low correlations between IVT and LPE or snow in the central Wasatch. Extreme LPE can be produced during periods with high *or* low IVT or TIVT (Fig. 14b). In this section, we examine if climatologically high IVT is a good indicator of an LPE extreme, focusing on periods when IVT $\geq$ 200 kg m^{-1} s^{-1} in the central Wasatch (roughly the 99th percentile of IVT for that location) at the midpoint of a 12-h observing period. There were 112 of such periods and 37 produced *no* LPE at CLN, while only 19 resulted in an LPE extreme. Thus, climatologically high IVT alone is not sufficient to anticipate an LPE extreme at CLN.

To understand what distinguishes high-IVT LPE extremes from those with no precipitation, we compared atmospheric profiles from the two event types. High IVT periods that produced extreme LPE were colder than those that did not produce LPE, with median temperatures ~10°C lower throughout the atmosphere for the former, a difference that was statistically significant throughout the entire atmospheric column (Fig. 16a). Consistent with these lower temperatures, the high IVT periods that produced extreme LPE featured lower specific humidity but higher relative humidity, the difference in the latter being statistically significant up to 425 hPa (Figs. 16b,c). The larger subsaturations in high IVT periods which produced no LPE are simply less favorable for precipitation development, despite the high IVT. The high IVT extreme LPE events also had higher wind speeds, although the difference was not statistically significant (Fig. 16d). In both cases, low-level winds (i.e., below ~650 hPa) veer with height, consistent with warm-air advection if the flow is near geostrophic, but events with precipitation have a stronger meridional component and thus may be less influenced by the Oquirrh Range to the west, though that difference is not statistically significant (Fig. 16e). Last, vertical velocities are shifted toward higher upward values during high IVT periods that produce extreme LPE, especially near and above crest level (~650–600 hPa), where the differences are statistically significant (Fig. 16f). The ~31-km grid spacing of the ERA5 does not resolve the narrow Wasatch Range. Instead, a gradual slope extends across much of northern Utah. Therefore, we suggest that this enhanced upward motion reflects Rossby wave and frontogenetical forcing during extreme LPE periods (Fig. 16f). In summary, climatologically high IVT in the central Wasatch can be associated with extreme precipitation, but it is not a sufficient condition and can be associated with a wide range of possible outcomes. Additional environmental factors are needed to produce extreme LPE, including a near-saturated environment and large-scale ascent.

f. *Radar characteristics*

We conclude our analysis by presenting statistics from the KMTX radar. We produced plots of the frequency of 0.5° radar echoes $\geq$ 10 dBZ for both snow and LPE extremes,

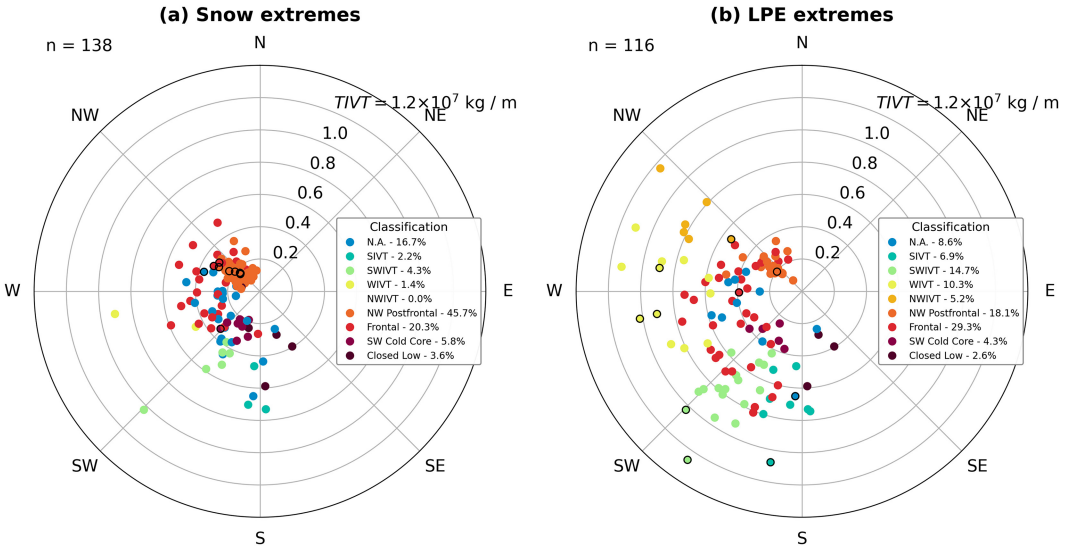

FIG. 14. Polar plots of TIVT and 700-hPa wind direction for all (a) snow extremes and (b) LPE extremes colored by synoptic classification. The 10 largest events are outlined in black.

binned by either 700-hPa flow direction or synoptic classification. The structure of these plots was similar for both snow and LPE extremes, so for brevity, we present LPE extremes. During periods with south-southwesterly and southwesterly flow, echo frequencies are highest over the Wasatch Range and down-radial areas not affected by beam blockage to the east. Relatively high echo frequencies are also present over the Stansbury and Oquirrh ranges and in some surrounding lowland areas (Figs. 17a,b). The lowlands immediately west of the Wasatch Range also exhibit higher frequencies, although the Stansbury and Oquirrh ranges and/or the Traverse Range between the Stansbury and Oquirrh ranges or Oquirrh and Wasatch ranges appear to produce some precipitation shadowing, in the form of reduced echo frequencies, over portions of the Tooele and Salt Lake Valleys (see Fig. 1b for geographic features). This suggests that these events frequently occur in the presence of a broader-scale precipitation system with embedded orographic precipitation enhancement over the Wasatch and other mountain ranges and lowland precipitation rates modulated by local terrain features. In west-southwesterly flow, high echo frequencies cover a broad region, with less modulation between the mountains and the lowlands, consistent with the presence of a front or large-scale forcing (Fig. 17c). In westerly flow, echo frequencies are greatest over the Stansbury, Oquirrh, and Wasatch ranges; lowlands to the immediate west (i.e., upstream) of the Wasatch Range; and down-radial areas to the east of the Wasatch Range not affected by beam blockage (Fig. 17d). Enhanced echo frequencies in the lowlands upstream of the Wasatch may reflect the influence of terrain-trapped airflows related to blocking and other orographic processes or

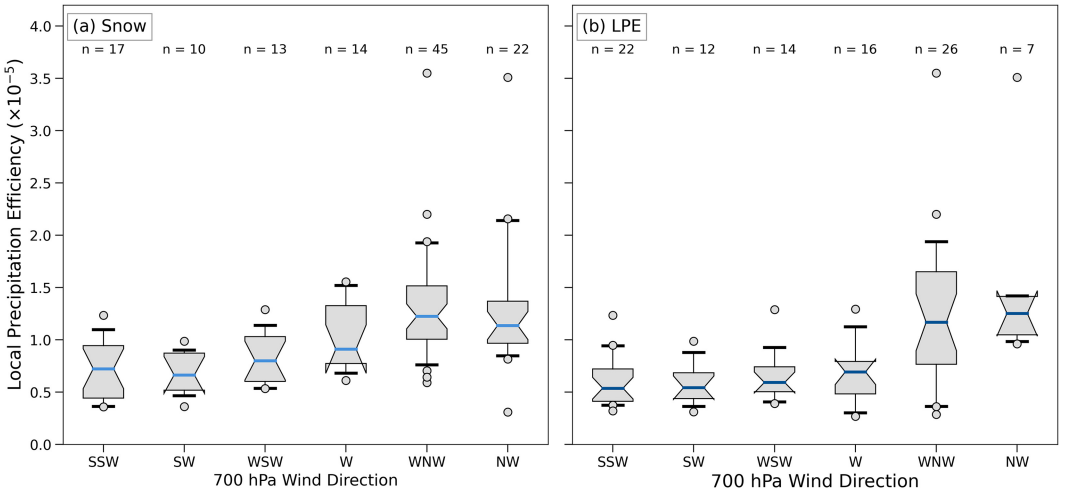

FIG. 15. As in Fig. 8, but for Local Precipitation Efficiency.

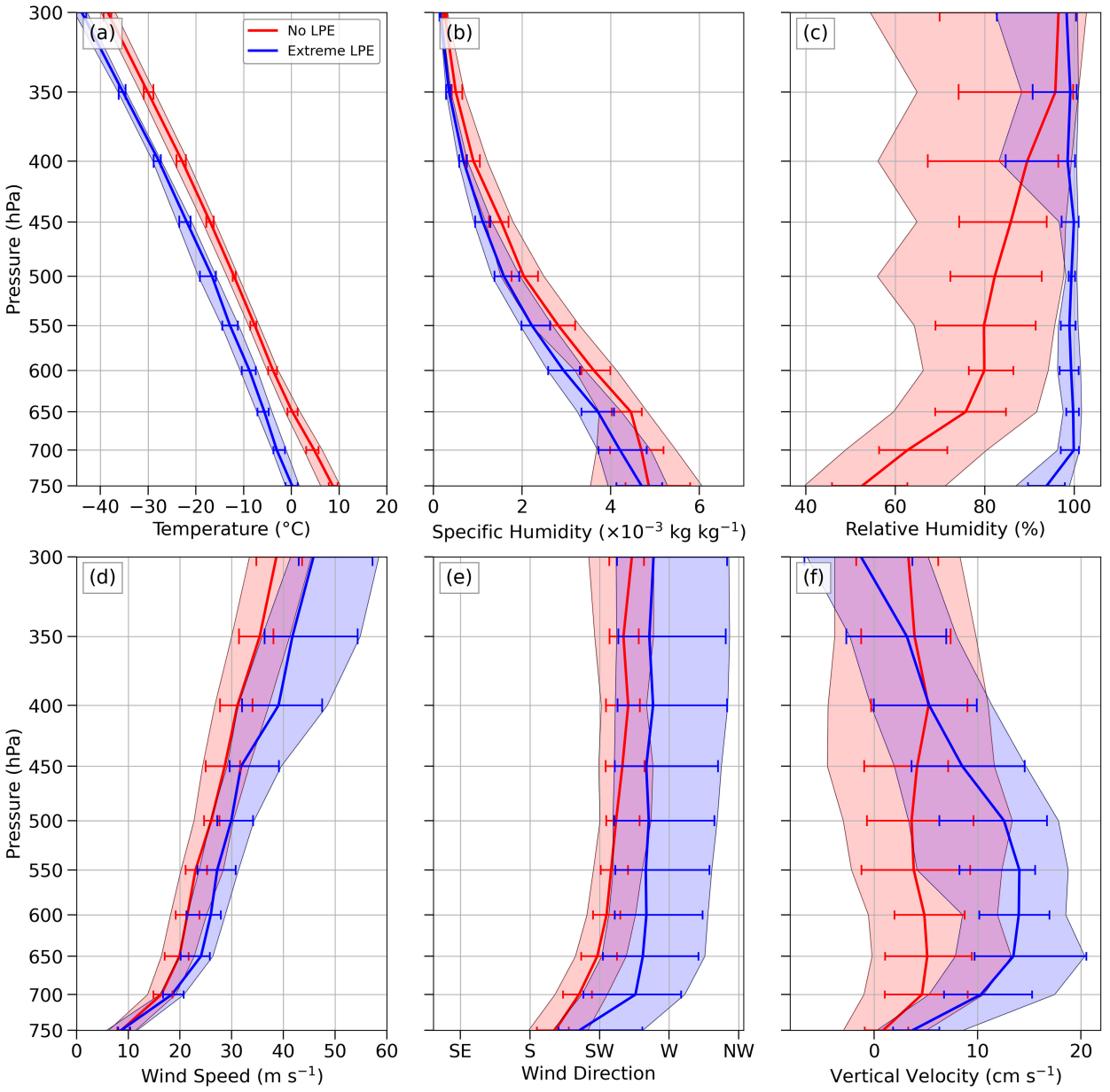

FIG. 16. Atmospheric profiles for periods with IVT ≥ 200 kg m^{-1} s^{-1} and no LPE (red; n = 37) and extreme LPE (blue; n = 19) at CLN. Solid colored lines indicate median values, and shading indicates the interquartile range. The whiskers show the 95% confidence interval of the median, based on bootstrap resampling with 5000 samples. (a) Temperature. (b) Specific humidity. (c) Relative humidity. (d) Wind speed. (e) Wind direction. (f) Vertical velocity.

upstream tilting mountain waves (e.g., Cox et al. 2005; Colle et al. 2005; Valenzuela and Kingsmill 2015, 2017; Ryoo et al. 2020), with some modulation by the upstream Stansbury and Oquirrh ranges (e.g., see the lower echo frequency immediately east and downstream of the Stansbury and Oquirrh ranges). Finally, for west-northwesterly and northwesterly flow, echoes are more confined to over the central Wasatch and the lowland region *immediately upstream* (Figs. 17d,e), indicating highly localized enhancement of postfrontal orographic or lake-effect convection.

The frequency of 0.5° radar echoes ≥ 10 dBZ for each synoptic classification provides another perspective. During the SIVT and NWIVT events, the greatest frequency of radar echoes ≥ 10 dBZ is in the Wasatch Range (Figs. 18a,d). In the case of SIVT, echo frequencies are much higher in the central Wasatch than in the northern or southern Wasatch Range. During the SWIVT and WIVT periods, the Wasatch Range still features the highest echo frequencies, but the echo frequencies are also locally high over portions of the Stansbury and Oquirrh ranges, and during WIVT, there is significant coverage in

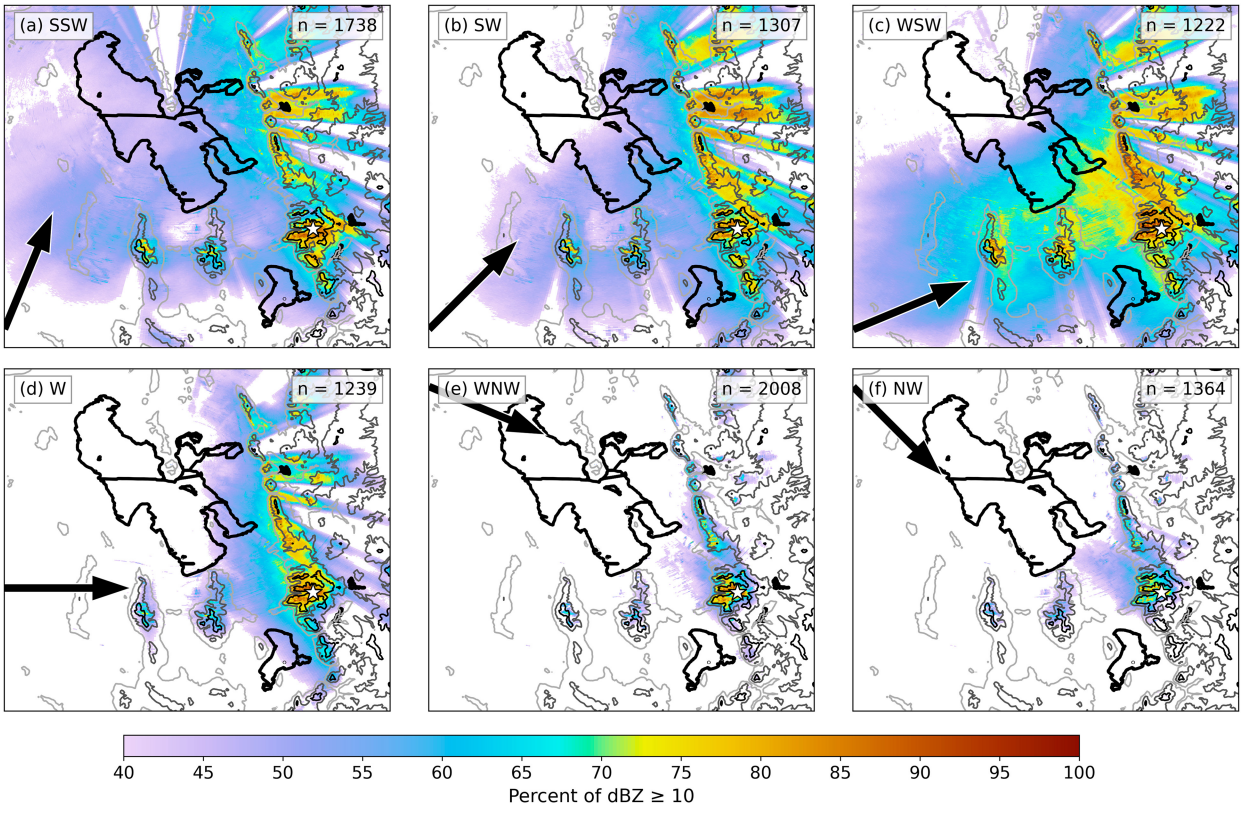

FIG. 17. Frequency of 0.5° radar echoes ≥ 10 dBZ (%; scale at bottom) for radar scans occurring during LPE extremes with (a) south-southwesterly, (b) southwesterly, (c) west-southwesterly, (d) westerly, (e) west-northwesterly, and (f) northwesterly 700-hPa winds. Thick black lines outline lakes. Thin contours display terrain height every 500 m from 1200 to 2700 m MSL. Black arrow displays the prevailing 700-hPa flow direction, and the white star denotes CLN. The number of radar scans used to produce the plot is in the top right.

the lowlands well upstream of the Wasatch Range (cf. Figs. 18b,c and 18a,d). NW Postfrontal storms have radar echoes confined to over and immediately upstream of the central Wasatch (Fig. 18e); the radar structure for these storms is similar to the plots for west-northwesterly and northwesterly flow (Figs. 17e,f), indicating the predominance of orographic and lake-effect convection during these periods and relatively infrequent concurrent occurrence of synoptic precipitation features. This is broadly consistent with Alcott et al. (2012) who found that GSL-effect precipitation occurred concurrently with synoptic stratiform precipitation only 10% of the time. Frontal events have the greatest coverage of ≥10 dBZ echoes with small variations between mountains and lowland areas (Fig. 18f). Thus, many of the Frontal events likely feature high LPE rates in the valleys as well as the mountains, consistent with Steenburgh (2003). The SW Cold Core statistics show enhancement over the Oquirrh, Stansbury, and Wasatch ranges, as well as over the lowlands upstream of the central Wasatch (over the Utah Valley) and the northern Wasatch (Fig. 18g).

The radar statistics described above indicate varied orographic and large-scale contributions to LPE extremes at CLN. Echo frequencies suggest many SIVT, SWIVT, NWIVT, and NW Postfrontal events feature relatively strong and, for some flow directions, localized enhancement of precipitation over and just upstream of the central Wasatch. In contrast, during WIVT and especially Frontal events, valley and lowland echo frequencies are higher, suggesting an important contribution from large-scale forcing. Although not a focus of this research, the above analyses also provide insights into the modulation of lowland precipitation, which can be confined to near the central Wasatch during the SIVT, SWIVT, NWIVT, and NW Postfrontal periods, but exhibit wide coverage during periods with stronger large-scale forcing.

4. Conclusions

Using snow and LPE observations from the Alta-Collins (CLN) snow study plot at Alta Ski Area, this research examined the characteristics of extreme snowfall events in northern Utah's upper Little Cottonwood Canyon (LCC), which can contribute to dangerous avalanche conditions that force the closure of State Route 210 (SR-210) and threaten lives and property in the town of Alta and village of Snowbird. During the 2000–22 cool-season (October–April) study period, there was an average of 117.7 12-h periods with ≥2.54 cm of new snow at CLN, the largest of which produced nearly 65 cm of snow. Almost all precipitation at CLN falls as snow during the cool season, with the median snow-to-liquid ratio (SLR)

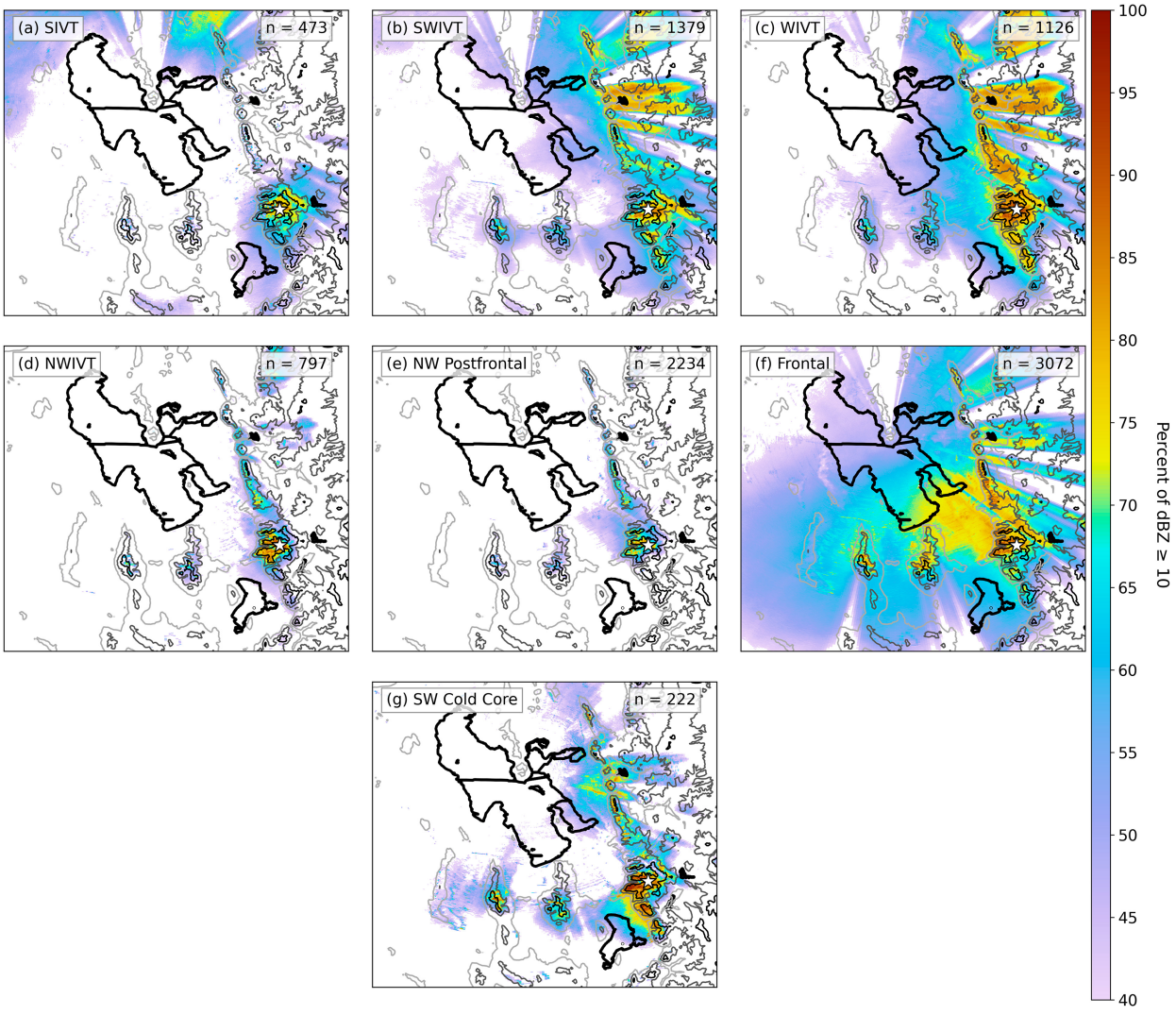

FIG. 18. As in Fig. 17, but for the (a) SIVT, (b) SWIVT, (c) WIVT, (d) NWIVT, (e) NW Postfrontal, (f) Frontal, and (g) SW Cold Core synoptic classifications.

of 12.8, characteristic of an intermountain snow climate. Extreme events, defined as the 95th percentile of 12-h new snow or liquid precipitation equivalent (LPE), exceeded 30.5 cm and 27.9 mm, respectively.

A wide range of flow directions are associated with extreme snowfall events in upper LCC. Snow extremes occur most frequently in west-northwesterly and northwesterly flow, while LPE extremes exhibit a bimodality in the flow direction frequency, with maxima for west-northwesterly and south-southwesterly flow. The LPE extreme bimodality contrasts with the modal distribution found over some broad, quasi-linear mountain barriers like the Cascade Range or Sierra Nevada (e.g., Pandey et al. 1999, see their Fig. 5; Yuter et al. 2011, see their Fig. 2) and appears to reflect shadowing by the Stansbury and Oquirrh ranges to the west, the influence of the Great Salt Lake and terrain-forced convergence due to the presence of the Oquirrh Range during northwesterly flow (Alcott and Steenburgh 2013), and the three-dimensional topography of the central Wasatch, which includes zonally oriented subbarrier ridges that yield upslope flow from a wide range of flow directions. The primacy of the west-northwesterly to northwesterly flow maximum for snow extremes reflects SLR, which is higher in west-northwesterly–northwesterly storms due to the lower temperatures associated with those flow directions.

Heavy snowfall in LCC is produced by diverse synoptic patterns. We identified eight synoptic classifications that generate snowfall extremes including four associated with high IVT from the south, southwest, west, and northwest (SIVT, SWIVT, WIVT, and NWIVT, respectively), post-cold-frontal northwesterly flow (NW Postfrontal), cold fronts or baroclinic troughs (Frontal), south-southwesterly cold core flow (SW Cold Core), and closed low pressure systems (Closed Low). IVT penetration for the high IVT patterns occurs to the north or south of the southern high Sierra and features relatively high 700-hPa (crest-level) winds and

temperatures, which, despite producing high LPE, frequently leads to modest snowfall totals due to low SLRs. Snow extremes occur most frequently during NW Postfrontal periods that are colder and often feature high SLRs.

Although some other mountainous regions such as California have a relatively high correlation between integrated water vapor transport (IVT) and LPE (e.g., Dettinger et al. 2011; Ricciotti and Cordeira 2022), the correlation over the western interior of the contiguous western United States is relatively low (see Rutz et al. 2014, their Fig. 2a). This more limited relationship between IVT and LPE is reflected in our analysis. Of the 112 periods with IVT $\geq$ 200 kg m^{-1} s^{-1} (roughly the 99th percentile) at the midpoint of a 12-h observing period, only 19 produced an LPE extreme and 37 produced *no* LPE at CLN. Comparison of events with these two outcomes indicates additional environmental factors are needed to produce extreme LPE, including a near-saturated environment (often with lower temperatures) and large-scale ascent. Additionally, in upper LCC, storms with low IVT can produce snow and LPE extremes, especially during NW Postfrontal events. The Local Precipitation Efficiency, defined as the ratio of precipitation to time-integrated IVT expressed as a water depth, is especially high during these periods, consistent with the efficient conversion of water vapor to precipitation in orographic convection or lake-effect storms.

Conditional radar statistics based on flow direction or synoptic classification indicate varied orographic and large-scale contributions to LPE extremes at CLN. Radar echo frequencies indicate localized enhancement of precipitation over and just upstream of the central Wasatch during SIVT, SWIVT, NWIVT, and NW Postfrontal events, whereas broader coverage occurs during WIVT and especially Frontal periods. In the case of the latter, the contrast in echo frequency from lowland to upland areas is relatively small, indicating that frontal periods exhibit weaker contrasts between lowland and mountain precipitation.

Although this research focused on the central Wasatch, it has broader implications for understanding orographic precipitation in other mountainous regions. Much of the prior work on orographic precipitation has focused on broad, quasi-linear mountain ranges, and orographic precipitation processes are often conceptualized using a single-ridge framework. The climatology for upper Little Cottonwood Canyon, however, illustrates how upstream topography and three-dimensional terrain geometries can complicate storm characteristics, orographic flow response, and precipitation processes. Although the Wasatch Range is generally long and narrow, the terrain of the *central Wasatch* broadens and has a nearly 1:1 horizontal aspect ratio (see Fig. 1c). We hypothesize that this terrain geometry exposes the central Wasatch to flow from multiple flow directions, with the high terrain of the northern and southern Wasatch Range limiting flow splitting. As a result, local orographic precipitation enhancement and extremes occur across a wide range of flow directions. Upstream ranges (i.e., the Oquirrh and Stansbury ranges), however, may limit the frequency of snowfall extremes during flow traversing those barriers. Finally, we illustrate that over interior mountainous regions, the relationship between IVT and precipitation may not be straightforward and show that during unstable postfrontal periods, the efficient conversion of water vapor to snow can lead to high snowfall rates despite relatively low IVT.

Overall, these results extend prior research by comprehensively describing the characteristics of extreme snowfall events in upper LCC, illustrating the meteorology associated with these events from an LPE *and* snow perspective, and describing the complex linkages between IVT and LPE extremes at this *interior* mountain location. These results have implications for weather forecasting, avalanche hazard assessment, and road-weather maintenance in LCC. While this research elucidated the climatological characteristics of extreme snowfall in upper LCC, it does not provide insight into the *physical mechanisms* responsible for the heavy snowfall. Future work is needed to better understand these precipitation processes, including multiridge effects associated with broadly separated, serially arranged mountain ridges commonly found in the Great Basin (e.g., the Stansbury, Oquirrh, and Wasatch ranges) and finer-scale ridge-canyon corrugations within individual ranges (e.g., the Alpine, Cottonwood, and Wildcat ridges in the Central Wasatch). This could involve the use of high-resolution numerical simulations and collection of airborne cloud-radar observations to gain an understanding of the hydrometeor growth, transport, and fallout processes that make upper LCC one of the snowiest places in the interior western United States.

Acknowledgments. This material is based upon work supported by the National Science Foundation under Grants AGS-1929602 and AGS-2227071. Any opinions, findings, and conclusions or recommendations expressed in this material are those of the authors and do not necessarily reflect the views of the National Science Foundation. We thank David Schultz, Larry Dunn, Peter Veals, Jason Knievel, three anonymous reviewers, and the editor for scientific input and suggestions that significantly improved this manuscript; Alta Ski Area and Ski Patrol for collecting and providing the snow observations; and the University of Utah Center for High Performance Computing (CHPC) for computer support.

Data availability statement. The CLN snow observations used in this research are openly available from the University of Utah Research Data Repository (Wasserstein and Steenburgh 2023). The ERA5 reanalysis is available from the Copernicus Climate Change Service (Hersbach et al. 2018a,b). The NEXRAD radar data are available from Amazon Web Services (NOAA National Weather Service 1991; https://registry.opendata.aws/noaa-nexrad/).

REFERENCES

Alcott, T. I., and W. J. Steenburgh, 2010: Snow-to-liquid ratio variability and prediction at a high-elevation site in Utah's Wasatch Mountains. *Wea. Forecasting*, **25**, 323–337, https://doi.org/10.1175/2009WAF2222311.1.

——, and ——, 2013: Orographic influences on a Great Salt Lake–effect snowstorm. *Mon. Wea. Rev.*, **141**, 2432–2450, https://doi.org/10.1175/MWR-D-12-00328.1.

——, ——, and N. F. Laird, 2012: Great Salt Lake–effect precipitation: Observed frequency, characteristics, and associated environmental factors. *Wea. Forecasting*, **27**, 954–971, https://doi.org/10.1175/WAF-D-12-00016.1.

Baxter, M. A., C. E. Graves, and J. T. Moore, 2005: A climatology of snow-to-liquid ratio for the contiguous United States. *Wea. Forecasting*, **20**, 729–744, https://doi.org/10.1175/WAF856.1.

Bjerknes, J., 1966: A possible response of the atmospheric Hadley circulation to equatorial anomalies of ocean temperature. *Tellus*, **18A**, 820–829, https://doi.org/10.3402/tellusa.v18i4.9712.

——, 1969: Atmospheric teleconnections from the equatorial Pacific. *Mon. Wea. Rev.*, **97**, 163–172, https://doi.org/10.1175/1520-0493(1969)097<0163:ATFTEP>2.3.CO;2.

Blattenberger, G., and R. Fowles, 1995: Road closure to mitigate avalanche danger: A case study for little cottonwood canyon. *Int. J. Forecasting*, **11**, 159–174, https://doi.org/10.1016/0169-2070(94)02008-D.

Bordi, I., X. Zhu, and K. Fraedrich, 2016: Precipitable water vapor and its relationship with the standardized precipitation index: Ground-based GPS measurements and reanalysis data. *Theor. Appl. Climatol.*, **123**, 263–275, https://doi.org/10.1007/s00704-014-1355-0.

Campbell, L. S., W. J. Steenburgh, Y. Yamada, M. Kawashima, and Y. Fujiyoshi, 2018: Influences of orography and coastal geometry on a transverse-mode sea-effect snowstorm over Hokkaido Island, Japan. *Mon. Wea. Rev.*, **146**, 2201–2220, https://doi.org/10.1175/MWR-D-17-0286.1.

Capozzi, V., C. De Vivo, and G. Budillon, 2022: Synoptic control over winter snowfall variability observed in a remote site of Apennine Mountains (Italy), 1884–2015. *Cryosphere*, **16**, 1741–1763, https://doi.org/10.5194/tc-16-1741-2022.

Caracena, F., R. A. Maddox, L. R. Hoxit, and C. F. Chappell, 1979: Mesoanalysis of the big Thompson storm. *Mon. Wea. Rev.*, **107**, 1–17, https://doi.org/10.1175/1520-0493(1979)107<0001:MOTBTS>2.0.CO;2.

Carpenter, D. M., 1993: The lake effect of the Great Salt Lake: Overview and forecast problems. *Wea. Forecasting*, **8**, 181–193, https://doi.org/10.1175/1520-0434(1993)008<0181:TLEOTG>2.0.CO;2.

Casaretto, G., M. E. Dillon, P. Salio, Y. G. Skabar, S. W. Nesbitt, R. S. Schumacher, C. M. García, and C. Catalini, 2022: High-resolution NWP forecast precipitation comparison over complex terrain of the Sierras de Córdoba during RELAMPAGO-CACTI. *Wea. Forecasting*, **37**, 241–266, https://doi.org/10.1175/WAF-D-21-0006.1.

Cayan, D. R., K. T. Redmond, and L. G. Riddle, 1999: ENSO and hydrologic extremes in the western United States. *J. Climate*, **12**, 2881–2893, https://doi.org/10.1175/1520-0442(1999)012<2881:EAHEIT>2.0.CO;2.

Colle, B. A., J. B. Wolfe, W. J. Steenburgh, D. E. Kingsmill, J. A. W. Cox, and J. C. Shafer, 2005: High-resolution simulations and microphysical validation of an orographic precipitation event over the Wasatch Mountains during IPEX IOP3. *Mon. Wea. Rev.*, **133**, 2947–2971, https://doi.org/10.1175/MWR3017.1.

——, R. B. Smith, and D. A. Wesley, 2013: Theory, observations, and predictions of orographic precipitation. *Mountain Weather Research and Forecasting: Recent Progress and Current Challenges*, F. K. Chow, S. F. J. de Wekker, and B. J. Snyder, Eds., Springer, 291–344.

Conlan, M., and B. Jamieson, 2016a: Naturally triggered persistent deep slab avalanches in western Canada. Part I: Avalanche characteristics and weather trends from weather stations. *J. Glaciol.*, **62**, 243–255, https://doi.org/10.1017/jog.2016.1.

——, and ——, 2016b: Naturally triggered persistent deep slab avalanches in western Canada. Part II: Weather trends from model forecasts. *J. Glaciol.*, **62**, 256–269, https://doi.org/10.1017/jog.2016.2.

Cox, J. A. W., W. J. Steenburgh, D. E. Kingsmill, J. C. Shafer, B. A. Colle, O. Bousquet, B. F. Smull, and H. Cai, 2005: The kinematic structure of a Wasatch Mountain Winter Storm during IPEX IOP3. *Mon. Wea. Rev.*, **133**, 521–542, https://doi.org/10.1175/MWR-2875.1.

DeHart, J. C., and R. A. Houze Jr., 2017: Orographic modification of precipitation processes in Hurricane Karl (2010). *Mon. Wea. Rev.*, **145**, 4171–4186, https://doi.org/10.1175/MWR-D-17-0014.1.

Dettinger, M. D., F. M. Ralph, T. Das, P. J. Neiman, and D. R. Cayan, 2011: Atmospheric rivers, floods and the water resources of California. *Water*, **3**, 445–478, https://doi.org/10.3390/w3020445.

Dunn, L. B., 1983: Quantitative and spacial distribution of winter precipitation along Utah's Wasatch front. NOAA Tech. Memo. NWS WR-181, 83 pp., https://repository.library.noaa.gov/view/noaa/14115/noaa_14115_DS1.pdf.

Eidhammer, T., V. Grubišić, R. Rasmussen, and K. Ikdea, 2018: Winter precipitation efficiency of mountain ranges in the Colorado Rockies under climate change. *J. Geophys. Res. Atmos.*, **123**, 2573–2590, https://doi.org/10.1002/2017JD027995.

Farestveit, N., and S. Skutlaberg, 2009: Experiences on a storm causing avalanche cycles in South-West Norway. *Proc. Int. Snow Science Workshop*, Davos, Switzerland, Montana State University, 567–571, https://arc.lib.montana.edu/snow-science/objects/issw-2009-0567-0571.pdf.

Foehn, P., M. Stoffel, and P. Bartelt, 2002: Formation and forecasting of large (catastrophic) new snow avalanches. *Int. Snow Science Workshop Proc. 2002*, Penticton, British Columbia, Canada, Montana State University, 141–148, https://arc.lib.montana.edu/snow-science/objects/issw-2002-141-148.pdf.

Foresti, L., I. V. Sideris, L. Panziera, D. Nerini, and U. Germann, 2018: A 10-year radar-based analysis of orographic precipitation growth and decay patterns over the Swiss Alpine region. *Quart. J. Roy. Meteor. Soc.*, **144**, 2277–2301, https://doi.org/10.1002/qj.3364.

Froidevaux, P., and O. Martius, 2016: Exceptional integrated vapour transport toward orography: An important precursor to severe floods in Switzerland. *Quart. J. Roy. Meteor. Soc.*, **142**, 1997–2012, https://doi.org/10.1002/qj.2793.

Hersbach, H., and Coauthors, 2018a: ERA5 hourly data on pressure levels from 1940 to present. Copernicus Climate Change Service (C3S) Climate Data Store (CDS), accessed 3 February 2023, https://doi.org/10.24381/cds.bd0915c6.

——, and Coauthors, 2018b: ERA5 hourly data on single levels from 1940 to present. Copernicus Climate Change Service (C3S) Climate Data Store (CDS), accessed 3 February 2023, https://doi.org/10.24381/cds.adbb2d47.

——, and Coauthors, 2020: The ERA5 global reanalysis. *Quart. J. Roy. Meteor. Soc.*, **146**, 1999–2049, https://doi.org/10.1002/qj.3803.

Hilker, N., A. Badoux, and C. Hegg, 2009: The Swiss flood and landslide damage database 1972–2007. *Nat. Hazards Earth Syst. Sci.*, **9**, 913–925, https://doi.org/10.5194/nhess-9-913-2009.

Horel, J. D., and J. M. Wallace, 1981: Planetary-scale atmospheric phenomena associated with the Southern Oscillation. *Mon. Wea. Rev.*, **109**, 813–829, https://doi.org/10.1175/1520-0493(1981)109<0813:PSAPAW>2.0.CO;2.

——, and C. V. Gibson, 1994: Analysis and simulation of a winter storm over Utah. *Wea. Forecasting*, **9**, 479–494, https://doi.org/10.1175/1520-0434(1994)009<0479:AASOAW>2.0.CO;2.

Houze, R. A., Jr., 2012: Orographic effects on precipitating clouds. *Rev. Geophys.*, **50**, RG1001, https://doi.org/10.1029/2011RG000365.

——, C. N. James, and S. Medina, 2001: Radar observations of precipitation and airflow on the Mediterranean side of the Alps: Autumn 1998 and 1999. *Quart. J. Roy. Meteor. Soc.*, **127**, 2537–2558, https://doi.org/10.1002/qj.49712757804.

Jag, J., 2023: Avalanche chaos causes Cottonwood Canyon closures, strands thousands. *Salt Lake Tribune*, 5 April, https://www.sltrib.com/sports/2023/04/05/avalanche-chaos-causes-cottonwood/.

James, C. N., and R. A. Houze Jr., 2005: Modification of precipitation by coastal orography in storms crossing northern California. *Mon. Wea. Rev.*, **133**, 3110–3131, https://doi.org/10.1175/MWR3019.1.

Johnston, E. C., F. V. Davenport, L. Wang, J. K. Caers, S. Muthukrishnan, M. Burke, and N. S. Diffenbaugh, 2021: Quantifying the effect of precipitation on landslide hazard in urbanized and non-urbanized areas. *Geophys. Res. Lett.*, **48**, e2021GL094038, https://doi.org/10.1029/2021GL094038.

Jong, B.-T., M. Ting, and R. Seager, 2016: El Niño's impact on California precipitation: seasonality, regionality, and El Niño intensity. *Environ. Res. Lett.*, **11**, 054021, https://doi.org/10.1088/1748-9326/11/5/054021.

Judson, A., and N. Doesken, 2000: Density of freshly fallen snow in the Central Rocky Mountains. *Bull. Amer. Meteor. Soc.*, **81**, 1577–1588, https://doi.org/10.1175/1520-0477(2000)081<1577:DOFFSI>2.3.CO;2.

Kirshbaum, D. J., and R. B. Smith, 2008: Temperature and moist-stability effects on midlatitude orographic precipitation. *Quart. J. Roy. Meteor. Soc.*, **134**, 1183–1199, https://doi.org/10.1002/qj.274.

Lackmann, G. M., and J. R. Gyakum, 1999: Heavy cold-season precipitation in the northwestern United States: Synoptic climatology and an analysis of the flood of 17–18 January 1986. *Wea. Forecasting*, **14**, 687–700, https://doi.org/10.1175/1520-0434(1999)014<0687:HCSPIT>2.0.CO;2.

Lavers, D. A., and G. Villarini, 2013: The nexus between atmospheric rivers and extreme precipitation across Europe. *Geophys. Res. Lett.*, **40**, 3259–3264, https://doi.org/10.1002/grl.50636.

Lentink, H. S., C. M. Grams, M. Riemer, and S. C. Jones, 2018: The effects of orography on the extratropical transition of tropical cyclones: A case study of Typhoon Sinlaku (2008). *Mon. Wea. Rev.*, **146**, 4231–4246, https://doi.org/10.1175/MWR-D-18-0150.1.

Liu, M., and J. A. Smith, 2016: Extreme rainfall from landfalling tropical cyclones in the eastern United States: Hurricane Irene (2011). *J. Hydrometeor.*, **17**, 2883–2904, https://doi.org/10.1175/JHM-D-16-0072.1.

Lorente-Plazas, R., T. P. Mitchell, G. Mauger, and E. P. Salathé Jr., 2018: Local enhancement of extreme precipitation during atmospheric rivers as simulated in a regional climate model. *J. Hydrometeor.*, **19**, 1429–1446, https://doi.org/10.1175/JHM-D-17-0246.1.

Maddox, R. A., L. R. Hoxit, C. F. Chappell, and F. Caracena, 1978: Comparison of meteorological aspects of the big Thompson and Rapid City flash floods. *Mon. Wea. Rev.*, **106**, 375–389, https://doi.org/10.1175/1520-0493(1978)106<0375:COMAOT>2.0.CO;2.

Manabe, S., 1957: On the modification of air-mass over the Japan sea when the outburst of cold air predominates. *J. Meteor. Soc. Japan*, **35**, 311–326, https://doi.org/10.2151/jmsj1923.35.6_311.

Martinez-Villalobos, C., and J. D. Neelin, 2019: Why do precipitation intensities tend to follow gamma distributions? *J. Atmos. Sci.*, **76**, 3611–3631, https://doi.org/10.1175/JAS-D-18-0343.1.

Minder, J. R., D. R. Durran, G. H. Roe, and A. M. Anders, 2008: The climatology of small-scale orographic precipitation over the Olympic Mountains: Patterns and processes. *Quart. J. Roy. Meteor. Soc.*, **134**, 817–839, https://doi.org/10.1002/qj.258.

Mock, C. J., and K. W. Birkeland, 2000: Snow avalanche climatology of the western United States mountain ranges. *Bull. Amer. Meteor. Soc.*, **81**, 2367–2392, https://doi.org/10.1175/1520-0477(2000)081<2367:SACOTW>2.3.CO;2.

Nalli, B., and M. Mckee, 2018: How little Cottonwood Canyon got this way and what can be done to fix it. *Int. Snow Science Workshop Proc. 2018*, Innsbruck, Austria, Montana State University, 246–250, https://arc.lib.montana.edu/snow-science/item/2527.

Narsey, S., C. Jakob, M. S. Singh, M. Bergemann, V. Louf, A. Protat, and C. Williams, 2019: Convective precipitation efficiency observed in the tropics. *Geophys. Res. Lett.*, **46**, 13 574–13 583, https://doi.org/10.1029/2019GL085031.

NCEI, 2021: U.S. climate normals. NCEI, accessed 14 April 2023, https://www.ncei.noaa.gov/products/land-based-station/us-climate-normals.

Neiman, P. J., L. J. Schick, F. M. Ralph, M. Hughes, and G. A. Wick, 2011: Flooding in western Washington: The connection to atmospheric rivers. *J. Hydrometeor.*, **12**, 1337–1358, https://doi.org/10.1175/2011JHM1358.1.

NOAA National Weather Service, 1991: NOAA Next Generation Radar (NEXRAD) Level 2 base data. NOAA/NCEI, accessed 2 February 2023, https://doi.org/10.7289/V5W9574V.

Nöthiger, C., and H. Elsasser, 2004: Natural hazards and tourism: New findings on the European Alps. *Mt. Res. Dev.*, **24**, 24–27, https://doi.org/10.1659/0276-4741(2004)024[0024:NHATNF]2.0.CO;2.

Pandey, G. R., D. R. Cayan, and K. P. Georgakakos, 1999: Precipitation structure in the Sierra Nevada of California during winter. *J. Geophys. Res.*, **104**, 12 019–12 030, https://doi.org/10.1029/1999JD900103.

Ralph, F. M., P. J. Neiman, G. A. Wick, S. I. Gutman, M. D. Dettinger, D. R. Cayan, and A. B. White, 2006: Flooding on California's Russian river: Role of atmospheric rivers. *Geophys. Res. Lett.*, **33**, L13801, https://doi.org/10.1029/2006GL026689.

——, J. J. Rutz, J. M. Cordeira, M. Dettinger, M. Anderson, D. Reynolds, L. J. Schick, and C. Smallcomb, 2019: A scale to characterize the strength and impacts of atmospheric rivers. *Bull. Amer. Meteor. Soc.*, **100**, 269–289, https://doi.org/10.1175/BAMS-D-18-0023.1.

Redmond, K. T., and R. W. Koch, 1991: Surface climate and streamflow variability in the western United States and their relationship to large-scale circulation indices. *Water Resour. Res.*, **27**, 2381–2399, https://doi.org/10.1029/91WR00690.

Ricciotti, J. A., and J. M. Cordeira, 2022: Summarizing relationships among landfalling atmospheric rivers, integrated water vapor transport, and California watershed precipitation 1982–2019. *J. Hydrometeor.*, **23**, 1439–1454, https://doi.org/10.1175/JHM-D-21-0119.1.

Roe, G. H., 2005: Orographic precipitation. *Annu. Rev. Earth Planet. Sci.*, **33**, 645–671, https://doi.org/10.1146/annurev.earth.33.092203.122541.

Roebber, P. J., and J. R. Gyakum, 2003: Orographic influences on the mesoscale structure of the 1998 ice storm. *Mon. Wea. Rev.*, **131**, 27–50, https://doi.org/10.1175/1520-0493(2003)131<0027:OIOTMS>2.0.CO;2.

——, S. L. Bruening, D. M. Schultz, and J. V. Cortinas, 2003: Improving snowfall forecasting by diagnosing snow density. *Wea. Forecasting*, **18**, 264–287, https://doi.org/10.1175/1520-0434(2003)018<0264:ISFBDS>2.0.CO;2.

Ropelewski, C. F., and M. S. Halpert, 1986: North American precipitation and temperature patterns associated with the El Niño/Southern Oscillation (ENSO). *Mon. Wea. Rev.*, **114**, 2352–2362, https://doi.org/10.1175/1520-0493(1986)114<2352:NAPATP>2.0.CO;2.

Rowntree, P. R., 1972: The influence of tropical east Pacific Ocean temperatures on the atmosphere. *Quart. J. Roy. Meteor. Soc.*, **98**, 290–321, https://doi.org/10.1002/qj.49709841605.

Rutz, J. J., and W. J. Steenburgh, 2012: Quantifying the role of atmospheric rivers in the interior western United States. *Atmos. Sci. Lett.*, **13**, 257–261, https://doi.org/10.1002/asl.392.

——, ——, and F. M. Ralph, 2014: Climatological characteristics of atmospheric rivers and their inland penetration over the western United States. *Mon. Wea. Rev.*, **142**, 905–921, https://doi.org/10.1175/MWR-D-13-00168.1.

——, ——, and ——, 2015: The inland penetration of atmospheric rivers over western North America: A Lagrangian analysis. *Mon. Wea. Rev.*, **143**, 1924–1944, https://doi.org/10.1175/MWR-D-14-00288.1.

Ryoo, J.-M., and Coauthors, 2020: Terrain trapped airflows and precipitation variability during an atmospheric river event. *J. Hydrometeor.*, **21**, 355–375, https://doi.org/10.1175/JHM-D-19-0040.1.

Schaerer, P., 1989: The avalanche-hazard index. *Ann. Glaciol.*, **13**, 241–247, https://doi.org/10.3189/S0260305500007977.

Schweizer, J., J. Bruce Jamieson, and M. Schneebeli, 2003: Snow avalanche formation. *Rev. Geophys.*, **41**, 1016, https://doi.org/10.1029/2002RG000123.

——, C. Mitterer, and L. Stoffel, 2009: On forecasting large and infrequent snow avalanches. *Cold Reg. Sci. Technol.*, **59**, 234–241, https://doi.org/10.1016/j.coldregions.2009.01.006.

Shafer, J. C., and W. J. Steenburgh, 2008: Climatology of strong intermountain cold fronts. *Mon. Wea. Rev.*, **136**, 784–807, https://doi.org/10.1175/2007MWR2136.1.

Sinclair, M. R., 1993: A diagnostic study of the extratropical precipitation resulting from Tropical Cyclone Bola. *Mon. Wea. Rev.*, **121**, 2690–2707, https://doi.org/10.1175/1520-0493(1993)121<2690:ADSOTE>2.0.CO;2.

Smith, R. B., Q. Jiang, M. G. Fearon, P. Tabary, M. Dorninger, J. D. Doyle, and R. Benoit, 2003: Orographic precipitation and air mass transformation: An Alpine example. *Quart. J. Roy. Meteor. Soc.*, **129**, 433–454, https://doi.org/10.1256/qj.01.212.

——, P. Schafer, D. Kirshbaum, and E. Regina, 2009: Orographic enhancement of precipitation inside Hurricane Dean. *J. Hydrometeor.*, **10**, 820–831, https://doi.org/10.1175/2008JHM1057.1.

Steenburgh, W. J., 2003: One hundred inches in one hundred hours: Evolution of a Wasatch Mountain winter storm cycle. *Wea. Forecasting*, **18**, 1018–1036, https://doi.org/10.1175/1520-0434(2003)018<1018:OHIIOH>2.0.CO;2.

——, 2023: *Secrets of the Greatest Snow on Earth*. 2nd ed. Utah State University Press, 225 pp.

——, and S. Nakai, 2020: Perspectives on sea- and lake-effect precipitation from Japan's "Gosetsu Chitai." *Bull. Amer. Meteor. Soc.*, **101**, E58–E72, https://doi.org/10.1175/BAMS-D-18-0335.1.

——, S. F. Halvorson, and D. J. Onton, 2000: Climatology of lake-effect snowstorms of the Great Salt Lake. *Mon. Wea. Rev.*, **128**, 709–727, https://doi.org/10.1175/1520-0493(2000)128<0709:COLESO>2.0.CO;2.

Stoelinga, M. T., R. E. Stewart, G. Thompson, and J. M. Thériault, 2013: Microphysical processes within winter orographic cloud and precipitation systems. *Mountain Weather Research and Forecasting: Recent Progress and Current Challenges*, F. K. Chow, S. F. J. de Wekker, and B. J. Snyder, Eds., Springer, 345–408.

Stohl, A., C. Forster, and H. Sodemann, 2008: Remote sources of water vapor forming precipitation on the Norwegian West Coast at 60°N—A tale of hurricanes and an atmospheric river. *J. Geophys. Res.*, **113**, D05102, https://doi.org/10.1029/2007JD009006.

Sturdevant-Rees, P., J. A. Smith, J. Morrison, and M. L. Baeck, 2001: Tropical storms and the flood hydrology of the central Appalachians. *Water Resour. Res.*, **37**, 2143–2168, https://doi.org/10.1029/2000WR900310.

Sui, C.-H., X. Li, and M.-J. Yang, 2007: On the definition of precipitation efficiency. *J. Atmos. Sci.*, **64**, 4506–4513, https://doi.org/10.1175/2007JAS2332.1.

Trenberth, K. E., G. W. Branstator, D. Karoly, A. Kumar, N.-C. Lau, and C. Ropelewski, 1998: Progress during TOGA in understanding and modeling global teleconnections associated with tropical sea surface temperatures. *J. Geophys. Res.*, **103**, 14 291–14 324, https://doi.org/10.1029/97JC01444.

Valenzuela, R. A., and D. E. Kingsmill, 2015: Orographic precipitation forcing along the coast of northern California during a landfalling winter storm. *Mon. Wea. Rev.*, **143**, 3570–3590, https://doi.org/10.1175/MWR-D-14-00365.1.

——, and ——, 2017: Terrain-trapped airflows and orographic rainfall along the coast of northern California. Part I: Kinematic characterization using a wind profiling radar. *Mon. Wea. Rev.*, **145**, 2993–3008, https://doi.org/10.1175/MWR-D-16-0484.1.

Veals, P. G., W. J. Steenburgh, S. Nakai, and S. Yamaguchi, 2020: Intrastorm variability of the inland and orographic enhancement of a sea-effect snowstorm in the Hokuriku region of Japan. *Mon. Wea. Rev.*, **148**, 2527–2548, https://doi.org/10.1175/MWR-D-19-0390.1.

Viale, M., and M. N. Nuñez, 2011: Climatology of winter orographic precipitation over the subtropical Central Andes and associated synoptic and regional characteristics. *J. Hydrometeor.*, **12**, 481–507, https://doi.org/10.1175/2010JHM1284.1.

Wasserstein, M. L., and W. J. Steenburgh, 2023: Alta-Collins snow and liquid precipitation equivalent observations 2000–2023. Accessed 1 September 2023, https://toi.lib.utah.edu/resolve/10.7278/S50d-nsy5-8bje.

Whiteman, C. D., 2000: Mountain climates of North America. *Mountain Meteorology: Fundamentals and Applications*, C. D. Whiteman, Ed., Oxford University Press, 11–22.

Whittaker, L. M., and L. H. Horn, 1981: Geographical and seasonal distribution of North American cyclogenesis, 1958–1977. *Mon. Wea. Rev.*, **109**, 2312–2322, https://doi.org/10.1175/1520-0493(1981)109<2312:GASDON>2.0.CO;2.

Williams, P., Jr., and E. L. Peck, 1962: Terrain influences on precipitation in the Intermountain West as related to synoptic situations. *J. Appl. Meteor.*, **1**, 343–347, https://doi.org/10.1175/1520-0450(1962)001<0343:TIOPIT>2.0.CO;2.

Wolter, K., and M. S. Timlin, 2011: El Niño/Southern Oscillation behaviour since 1871 as diagnosed in an extended multivariate ENSO index (MEI.ext). *Int. J. Climatol.*, **31**, 1074–1087, https://doi.org/10.1002/joc.2336.

Wood, V. T., R. A. Brown, and S. V. Vasiloff, 2003: Improved detection using negative elevation angles for mountaintop WSR-88Ds. Part II: Simulations of the three radars covering

Utah. *Wea. Forecasting*, **18**, 393–403, https://doi.org/10.1175/1520-0434(2003)18<393:IDUNEA>2.0.CO;2.

Wulfmeyer, V., and Coauthors, 2011: The Convective and Orographically-induced Precipitation Study (COPS): The scientific strategy, the field phase, and research highlights. *Quart. J. Roy. Meteor. Soc.*, **137**, 3–30, https://doi.org/10.1002/qj.752.

Yeager, K. N., W. J. Steenburgh, and T. I. Alcott, 2013: Contributions of lake-effect periods to the cool-season hydroclimate of the Great Salt Lake basin. *J. Appl. Meteor. Climatol.*, **52**, 341–362, https://doi.org/10.1175/JAMC-D-12-077.1.

Yuter, S. E., D. A. Stark, J. A. Crouch, M. J. Payne, and B. A. Colle, 2011: The impact of varying environmental conditions on the spatial and temporal patterns of orographic precipitation over the Pacific Northwest near Portland, Oregon. *J. Hydrometeor.*, **12**, 329–351, https://doi.org/10.1175/2010JHM1239.1.

Zishka, K. M., and P. J. Smith, 1980: The climatology of cyclones and anticyclones over North America and surrounding ocean environs for January and July, 1950–77. *Mon. Wea. Rev.*, **108**, 387–401, https://doi.org/10.1175/1520-0493(1980)108<0387:TCOCAA>2.0.CO;2.